Carbon/carbon Composites for Next Generation Microvascular Solar Thermal Receivers

by

Matt Zuzelski

A thesis

submitted in partial fulfillment

of the requirements for the degree of

Master of Science in Mechanical Engineering

Boise State University

August 2023

BOISE STATE UNIVERSITY GRADUATE COLLEGE

DEFENSE COMMITTEE AND FINAL READING APPROVALS

of the thesis submitted by

Matt Zuzelski

Thesis Title: Carbon/carbon Composites for Next Generation Microvascular Solar Thermal Receivers

Date of Final Oral Examination: 05 May 2023

The following individuals read and discussed the thesis submitted by student Matt Zuzelski, and they evaluated the student's presentation and response to questions during the final oral examination. They found that the student passed the final oral examination.

Todd Otanicar, Ph.D.	Chair, Supervisory Committee
Krishna Pakala, Ph.D.	Member, Supervisory Committee
Mahmood Mamivand, Ph.D.	Member, Supervisory Committee
Marta Laporte-Azcué, Ph.D.	Member, Supervisory Committee

The final reading approval of the thesis was granted by Todd Otanicar, Ph.D., Chair of the Supervisory Committee. The thesis was approved by the Graduate College.

DEDICATION

None of this would have been possible without the enormous support from my Mom, Doback, and Ella. Thank you all for being there for me around every corner in this journey.

ACKNOWLEDGMENTS

I would like to thank Dr. Todd Otanicar for creating a valuable and fun research environment for me over these last 2 years. I have thoroughly enjoyed studying under your expertise and hope to continue learning from you in the future. I would also like to thank Madan Aryal and Jordan Loew for their work helping me in the lab.

I owe great thanks to the members of the research project at The University of Tulsa. In particular, Carlos Cordeiro for the fabrication of the carbon/carbon composites and Dr. Michael Keller.

This material is based upon work supported by the U.S. Department of Energy's Office of Energy Efficiency and Renewable Energy (EERE) under Solar Energy Technologies Offices (SETO) Agreement Number EE0008736.

ABSTRACT

Concentrating solar power (CSP) is a method of renewable solar power generation where the sun's radiant energy is collected by a receiver and converted into thermal energy. This thermal energy is then passed into a heat transfer fluid and either sent to thermal storage, or a steam power plant. One path to better CSP systems is improving the operational envelope of the receiver and heat transfer fluid (HTF) system by utilizing more resilient absorbing materials, different path architectures, and HTFs with higher allowable temperatures.

A new carbon/carbon composite is being developed with the potential to function as the absorbing material for a solar thermal receiver. This composite is capable of functioning at higher temperatures than current metallic receivers and could reduce the cost of the supporting structure due to its low density. This composite is readily coupled with microvascular ($D < 1mm$) channel structures by constructing channels with PLA and melting the plastic out at a later stage. The smaller channel diameters allow for HTF pairings that previously required excessive wall thickness such as supercritical CO_2 (sCO_2).

A series of computational fluid dynamics simulations have been conducted to first understand the operational limits of a single (20mm x 20mm) microscale receiver plate capable of thermal efficiency above 90%. Then, these plates are numbered up to create a full-scale receiver based on a design point from Gemasolar's flux profile with an estimated 85.04% thermal efficiency.

The carbon/carbon composite has been characterized for its thermal, optical, and aging properties. Thermal conductivity has been measured for the composite made with both PAN-based and pitch-based fibers where the pitch-based fibers had through plane thermal conductivity 478% higher than that of the PAN-based fibers. Then, the composite underwent an accelerated aging process via cyclic aging in a high flux solar simulator and isothermal aging in a tube furnace. The optical properties were characterized for the carbon/carbon composite throughout the aging processes.

TABLE OF CONTENTS

LIST OF TABLES

LIST OF FIGURES

LIST OF ABBREVIATIONS

CSP	Concentrating Solar Power
HTF	Heat Transfer Fluid
CFD	Computational Fluid Dynamics
UDF	User Defined Function
DOE	Department of Energy
CTE	Coefficient of Thermal Expansion
SST	Shear Stress Transport
PLA	Poly Lactic Acid

NOMENCLATURE

α_λ	Spectral Absorptance
ρ_λ	Spectral Reflectance
E_λ	ASTM G173-03 Reference Spectrum
α_{y81}	Solar Weighted Absorptance
k	Thermal Conductivity (W/m-K)
α	Thermal Diffusivity (m^2/s)
C_p	Specific Heat (J/kg-K)
ρ	Density (kg/m^3)
$q^{"}_{solar\ in}$	Solar Heat Flux into Receiver (kW/m^2)
$q^{"}_{rad\ in}$	Radiant Heat Flux into Receiver (kW/m^2)
$q^{"}_{rad\ out}$	Radiant Heat Flux out of Receiver (kW/m^2)
a	Absorptivity
$q^{"}_{solar}$	Solar Heat Flux (kW/m^2)
$q^{"}_{conv}$	Convective Heat Flux (kW/m^2)
$T_{ambient}$	Ambient Temperature (K)
$T_{surface}$	Receiver Surface Temperature (K)
ε	Emissivity
σ	Boltzmann Constant ($W/m^2\text{-}K^4$)
h	Heat Transfer Coefficient ($W/m^2\text{-}K$)
$q^{"}_{total}$	Total Heat Flux at Receiver Surface (kW/m^2)
η_{th}	Thermal Efficiency
$\dot{m}$	Mass Flow Rate (kg/s)

ΔT	Change in Temperature (K)
G	Solar Heat Flux (kW/m^2)
A	Receiver Absorbing Area (m^2)
E	Strain
α_{CTE}	Coefficient of Thermal Expansion (K^{-1})

CHAPTER ONE: INTRODUCTION

1.1 Background

Limited resources of fossil fuels coupled with concerns around climate change has led to global increases in the use and research of renewable energy for electrical power generation, one of which is utilizing the radiant energy from the sun [1]. Recently, solar energy has been a massively growing area of research whether through photovoltaic or solar thermal methods [2], [3]. Solar thermal power shows promise to gather significant amounts of energy via concentrated solar irradiation [4], [5]. Solar thermal power plants operate by reflecting sunlight onto a receiver, where the solar flux is converted into thermal energy. A heat transfer fluid (HTF) is pumped through the receiver to capture the thermal energy where it can then be coupled to a conventional power cycle to generate electricity. There are 4 primary concentrated solar power (CSP) configurations. Parabolic trough, linear Fresnel, parabolic dish, and power tower. Figure 1.1 shows these different configurations.

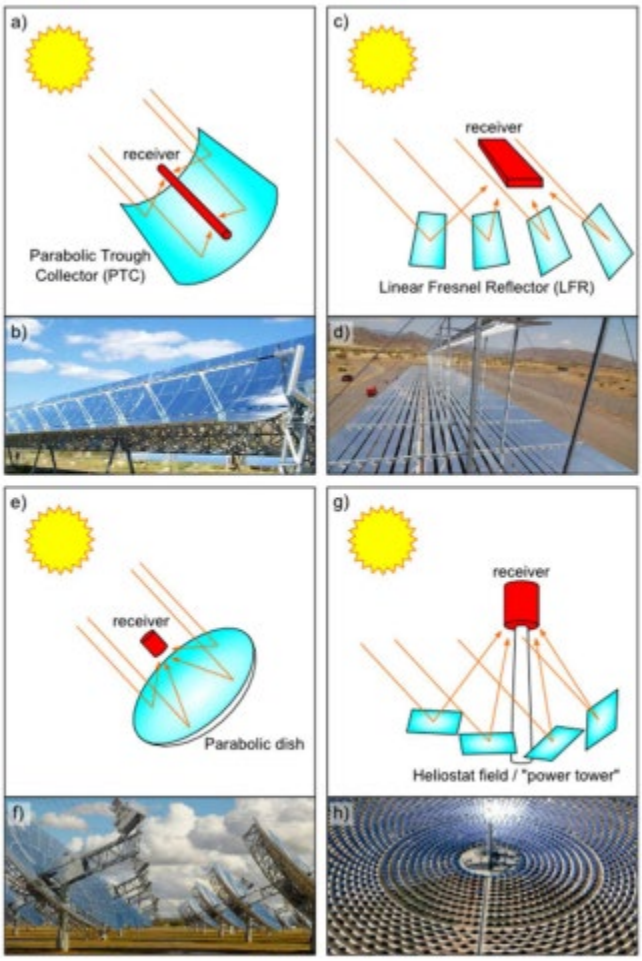

Figure 1.1 CSP Configurations for parabolic trough (a, b), linear Fresnel (c, d), parabolic dish (e, f), and power tower (g, h) plants [5]

The centralized tower approach is one where an array of mirrors (heliostats) focuses incoming solar energy onto a receiver located at the top of the tower, see Figure 1.1g. The receiver is a critical element of any solar tower design due to the overall impact on plant efficiency [6]. Current state-of-the-art receivers are metallic and utilize a molten salt external tubular design shown in Figure 1.2 [7]. There is debate as to whether metals or ceramics are more suitable as the absorbing material. The absorbing material should have high thermal shock resistance, high solar absorptance, and good oxidation resistance [8]. Since solar receivers are subjected to high temperatures, thermal shocks, and cycling,

ceramics and composites are excellent candidates due to their highly stable nature [9]. While metals are generally better at handling thermal differences from inconsistent solar fluxes due to their ductile nature, ceramics and composites can handle greater maximum temperatures leading to higher output temperatures and higher efficiencies that lead to decreased receiver size and cost of the supporting structure [10].

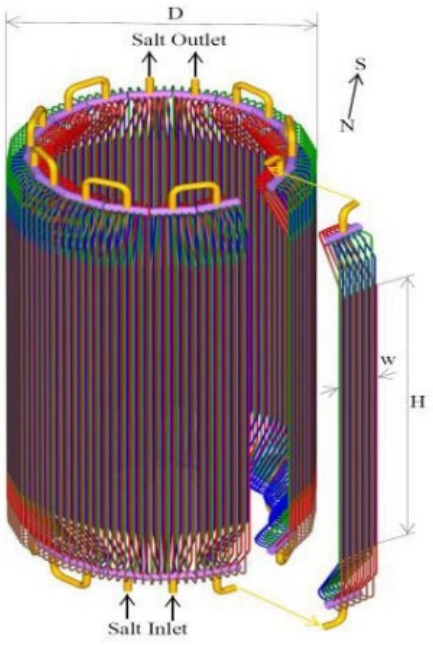

Figure 1.2 Tubular Molten Salt Receiver [7]

Current CSP systems can utilize solar flux levels up to 1 MW/m^2 [11] so producing receivers capable of operating at or above that level allows for receivers of reduced size and cost capable of the same power output. Microchannel heat exchangers ($D < 1$ mm) are historically highly efficient in thermal transfer and are well equipped to handle high operating pressures without excessively thick walls [12]. Utilizing a microchannel receiver structure also allows for testing of multiple types of HTFs including supercritical carbon dioxide (sCO_2), a working fluid of high interest due to its

application in the sCO_2 Brayton cycle [13], [14]. sCO_2 is capable of operation at temperatures above 600 °C where solar salt cannot be used. This space has potential for greater thermal efficiency [15], [16]. Supercritical carbon dioxide shows promise as a next generation working fluid but, requires a specialized receiver, like the example in Figure 1.3, and a heat exchanger to combine with traditional thermal storage systems. Molten salts are the more traditional approach to a heat transfer fluid as they can be used as the working fluid and as a thermal energy storage medium. Although, molten salts are corrosive and special care must be taken when choosing transport materials. Beyond this, liquid sodium is another impressive HTF due in large part to its high thermal conductivity. The higher conductivity allows for higher rates of heat transfer thus, permitting the use of smaller receivers with high flux densities [17].

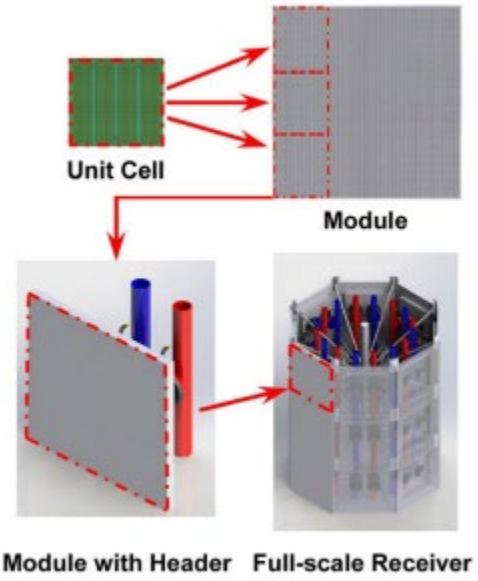

Figure 1.3 sCO_2 Microchannel Receiver from [12]

Carbon is typically known for its impressive mechanical characteristics and abundance of applications, such as carbon nanotubes, aircraft brakes, carbon fiber, and many others [18], [19]. This material is a good fit for a solar receiver as it is black in

color, making for potential high solar absorptance, and it is very resilient in withstanding thermal gradients which is necessary for high temperature solar receivers. Additionally, compared to other receiver materials, carbon is lightweight making the receiver cheaper to support [20]. Carbon-carbon composites, while impressive, require large amounts of processing to improve mechanical capabilities. These advanced materials are fabricated by combining carbon fibers with a carbonaceous matrix. Densification is required to fill voids within the matrix with carbon which also improves the integrity of the material [21]. Graphitization is typically the last step done to improve strength and thermal conductivity of the composite [22]. While these processes are integral to the success of the composite, they could affect the absorptance of the receiver which can be aided by a solar selective coating. Utilizing carbon-carbon composites for solar thermal receivers allows for increased flexibility in design due to the ability to build the composite around 3-D printed channels with PLA that is easily melted out at a later stage.

1.2 Research Goals and Objectives

Designing these receivers to operate efficiently and resiliently is a major step in the success of the overall system [6]. Hence, the target of this study is to understand the viability of a new carbon-carbon composite solar thermal receiver material option. This novel receiver concept consists of many microscale receiver modules. Each module is capable of housing complex path architectures that would otherwise be difficult to machine in traditional receiver materials. This new flexibility broadens the design space and allows for new designs that maximize thermal transfer and minimize pressure drop. This new space is somewhat unexplored and proper tools are required to efficiently test path designs and heat transfer fluid pairings.

To do this, the computational fluid dynamics (CFD) package ANSYS Fluent is used. CFD has shown itself to be advantageous in this type of simulation work [23], [24]. This novel microscale receiver utilizes microvascular channel structures, like those explored by [12]. Care is taken to pair this receiver with relatively new working fluids for the molten salt, gas, and metal categories as the heat transfer fluid can allow for larger operating ranges and reduced costs [12], [25], [26]. The composite will first be simulated as a single plate system, and then as a full-scale receiver, finally the carbon/carbon composite used in simulations can be characterized to compare with values used as parameters. Figure 1.4 visualizes this process. Focusing on the simpler, single plate system allows for streamlined understanding of the full-scale receiver system [12], [23], [24].

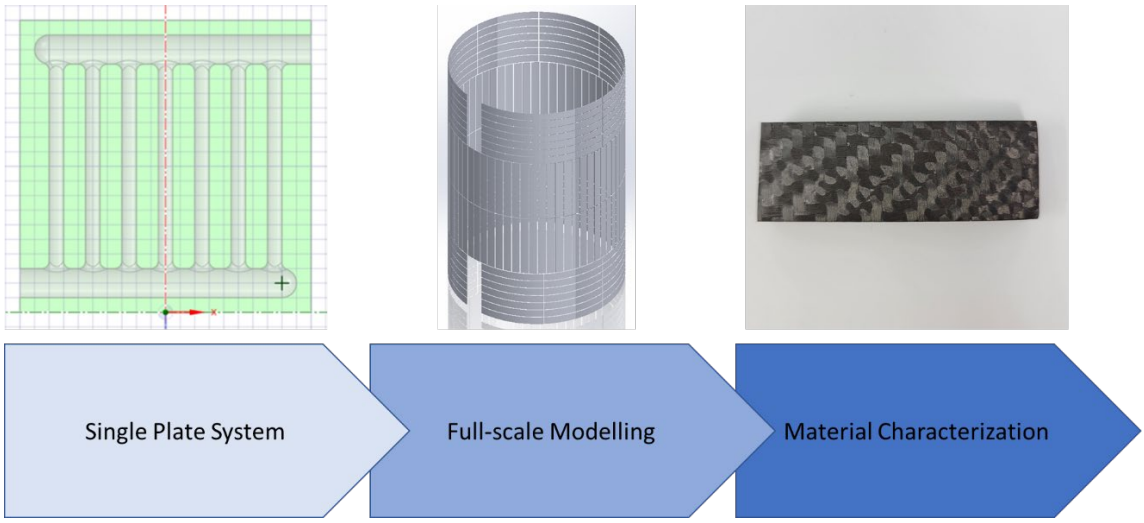

Figure 1.4 Study Goals Visualization

The carbon-carbon composite used in the simulated work is currently under development. Efforts are made to characterize optical and thermal properties for the composite and compare measured values with those used in simulations. Furthermore, solar thermal receivers operate in extreme conditions and degradation of the absorbing

material is a concern. Accelerated aging of the carbon-carbon composite is conducted to further understand the resiliency of the thermomechanical and optical properties after withstanding temperatures above 800 °C, focused UV exposure, and temperature fluctuations similar to that experienced by a solar thermal receiver.

CHAPTER TWO: EXPERIMENTAL METHODS

2.1 Carbon-carbon Composite Samples Fabrication

To fabricate the carbon-carbon (C/C) composites evaluated in this work, an autoclave was used to first produce a prepreg by combining PAN-based woven carbon fibers and a commercially available phenolic resin (BK 5236H, Bakelite Synthetics) with added resorcinol [27]. The micro-channels can be implemented during the prepreg fabrication stage by using a VaSC (vaporization of sacrificial component) technique, where poly lactic acid (PLA) is 3D printed into the desired channel network and later removed by a heat treatment under vacuum [28]. The prepregs were then sectioned into the desired size and sent to a heat treatment at 1000 °C under atmospheric argon (Ar) to promote carbonization. Chemical vapor infiltration (CVI) with methane at 1000 °C and a vacuum pressure of 250 mbar was used to densify the composite for up to 100 hours. After densification, the C/C composite samples were hand sanded using a 300 grit SiC paper to remove the external carbon deposits on the surface. A final graphitization step at 2200 °C under Ar was done to convert the initially amorphous carbon matrix into a crystalline graphite matrix.

Then, the carbon composite must be protected so the material does not burn at the extreme temperatures that are experienced. This is done with a pack cemented SiC buffer layer topped with a ZrB_2 layer. The SiC buffer layer halts the conversion of the carbon matrix further into the composite so the coating does not spread far into the thickness of the specimen. Once the coating is applied, the sample must undergo a curing process to ensure the integrity of the protective layer. In turn, this forms a protective shield for the carbon-carbon composite that allows for temperatures over 1000 °C.

2.2 Carbon/carbon Composite Characterization Methodology

2.2.1 Optical Properties

The carbon/carbon composite is characterized for solar weighted absorptance. To characterize this, the UV-2600 Shimadzu UV-Vis spectrophotometer with an integrating sphere is first used to measure the specimen spectral reflectance from 300 to 1400 nm. The data can then be converted to spectral absorptance via Eq. (2.1).

$$\alpha_\lambda = 1 - \rho_\lambda \tag{2.1}$$

Where α_λ is the spectral absorptance and ρ_λ is the spectral reflectance.

The solar weighted absorptance is then calculated as a numeric integral using the trapezoidal integration method. Eq. (2.2) shows the required integral [29].

$$\alpha_{y81} = \frac{\int_{300}^{1400} \alpha_\lambda E_\lambda \, d\lambda}{\int_{300}^{1400} E_\lambda \, d\lambda} \tag{2.2}$$

Where α_{y81} is the solar weighted absorptance and E_λ is the ASTM G173-03 reference spectrum for direct normal irradiance.

2.2.2 Pyromark Coating

The Pyromark coating method is based around an existing method [30]. The currently utilized method is described in Table 2.1 along with the curing schedule shown in Figure 2.1. These methods are used because they yield the most stable results, all Pyromark coated samples in this study are coated using this technique.

Table 2.1 Accelerated Aging Parameters and Sample Distribution

Step	Description
1	Dip uncured specimen for 1 coat
2	Let coat dry > 24 hours
3	Cure in tube furnace (see curing schedule)

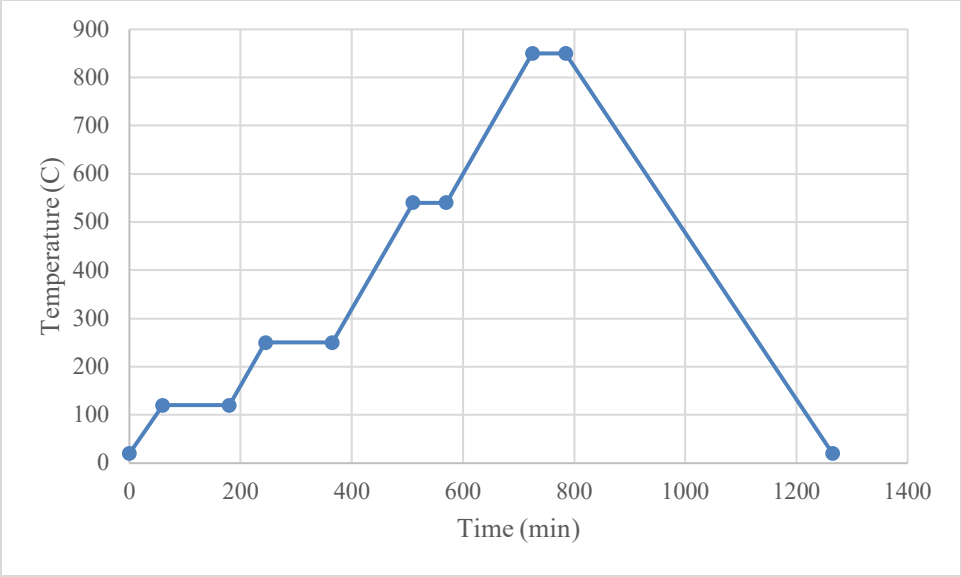

Figure 2.1 Furnace Curing Schedule for Pyromark

2.2.3 Thermal Conductivity Measurement

Five samples are measured for thermal conductivity in this study and are summarized in Table 2.2. The first 3 samples are fabricated samples using PAN-based fibers and represent different stages of processing. These stages are representative of the processing required to produce a functional sample that would be used as an absorbing material in a solar thermal receiver. Then, there is a commercial sample from Across Composites that claims a thermal conductivity of about 15 W/m-K. Lastly, another fabricated sample using pitch-based fibers that claim to be more conductive than PAN-based fibers.

Table 2.2 Samples Used for Thermal Conductivity Measurements

Sample Number	Fiber Type	Processing
1	PAN-based	Carbonized
2	PAN-based	Carbonized-CVI Densified
3	PAN-based	Carbonized-CVI Densified-Graphitized
4	Commercial	N/A
5	Pitch-based	Carbonized-CVI Densified-Graphitized

3 measurements are required to calculate thermal conductivity. First, the specimen is placed in a Linseis LFA1000 for a thermal diffusivity measurement via laser flash analysis. The measurements are done at 100°C intervals from room temperature to 800°C for the PAN-based fibers and at room temperature only for pitch-based fibers and the commercial sample. Then, the specific heat of the PAN-based samples is characterized on the DSC-2500 by using differential scanning calorimetry. These measurements were conducted up to 390°C due to equipment limitations. The density of the specimen is calculated via Archimedes' technique at room temperature as well. Eq. (2.3) shows how these values are combined to calculated the thermal conductivity of the specimen.

$$k = \alpha C_p \rho \tag{2.3}$$

Where k is the thermal conductivity, α is the thermal diffusivity, C_p is the specific heat, and ρ is the density.

2.2.4 High Flux Solar Simulator Aging Methods

A high flux solar simulator (HFSS) was developed based on work at Sandia [31]. The HFSS consists of four 1.8 kW metal halide arc lamps focused onto a point by ellipsoidal reflectors shown in Figure 2.2. The incident heat flux of the lamps was characterized individually and in pairs at the point of focus using the Hukseflux GG01

heat flux sensor. The measured flux values can be seen in Table 2.3 for lamps numbered 1 through 4.

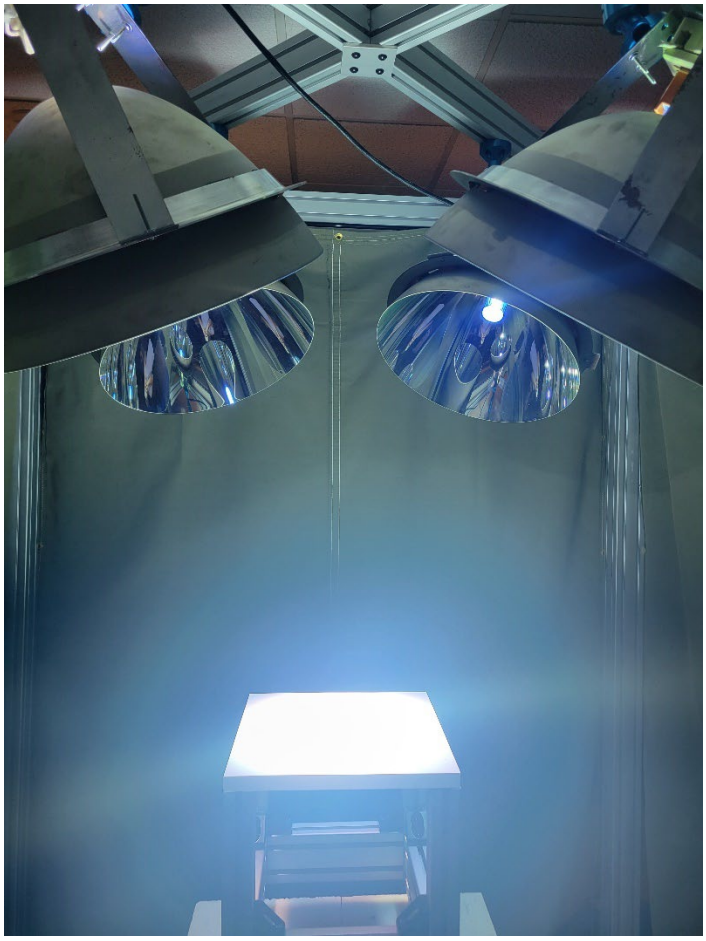

Figure 2.2 High Flux Solar Simulator Visual

Table 2.3 Measured Heat Flux for HFSS Lamp Configurations

Active Lamp Numbers	Heat Flux (kW/m^2)
1	177.8
2	161.1
3	130.8
4	139.9
1, 2	341.8
1, 2, 3	484.8
1, 2, 3, 4	641.5

Then, the HFSS was outfitted with a shutter that could be controlled on a timer. This timing is adjusted based on temperature measurements from a Micro-Epsilon CSLM-2LFF laser pyrometer aimed at the back of any sample placed in the HFSS. This pyrometer is capable of measuring temperatures from 250 °C to 800 °C. The timing for the shutter was adjusted until the samples could be cycled up to about 800 °C and down to about 320 °C. The sample is characterized for changes in mass and optical properties first after every 5, then 10, then 20 cycles. This experiment used one SiC coated carbon/carbon composite sample.

2.2.5 Isothermal Tube Furnace Aging Methods

Aging was also conducted for the samples via an isothermal method in the MTI GSL-1100X tube furnace. This method consists of placing samples into the tube furnace, heating the samples up to 850 °C, and holding at this temperature for 100 hours at a time. After every 100 hours, the samples are characterized for changes in mass and optical properties.

2.3 Carbon/carbon Composite Characterization Results

2.3.1 Optical Property Analysis

Optical properties were characterized for 4 carbon/carbon composite samples described in Table 2.4. The intent was to describe how the stages of processing affect the optical properties of the composite and compare these properties to a commercial sample from Across Composites. Importantly, these samples are not capable of withstanding the high temperatures experienced in a solar thermal receiver as they do not have a fire protective coating.

Table 2.4 Unprotected Sample Descriptions for Optical Property Measurements

Specimen	Process
1	Carbonized
2	Carbonized – Graphitized
3	Carbonized – Graphitized – CVI Densified
4	Across Composites Sample (N/A)

Each sample was measured for spectral reflectance. Results from these measurements are shown in Figure 2.3. Generally, the fabricated carbon-carbon composite has a similar spectral reflectance to the commercial sample. The slopes of the spectral reflectance profiles are similar and values are within 10 % of each other. Note that the sudden change in reflectance at 800 nm is due to the UV-VIS swapping detectors and is not caused by the material.

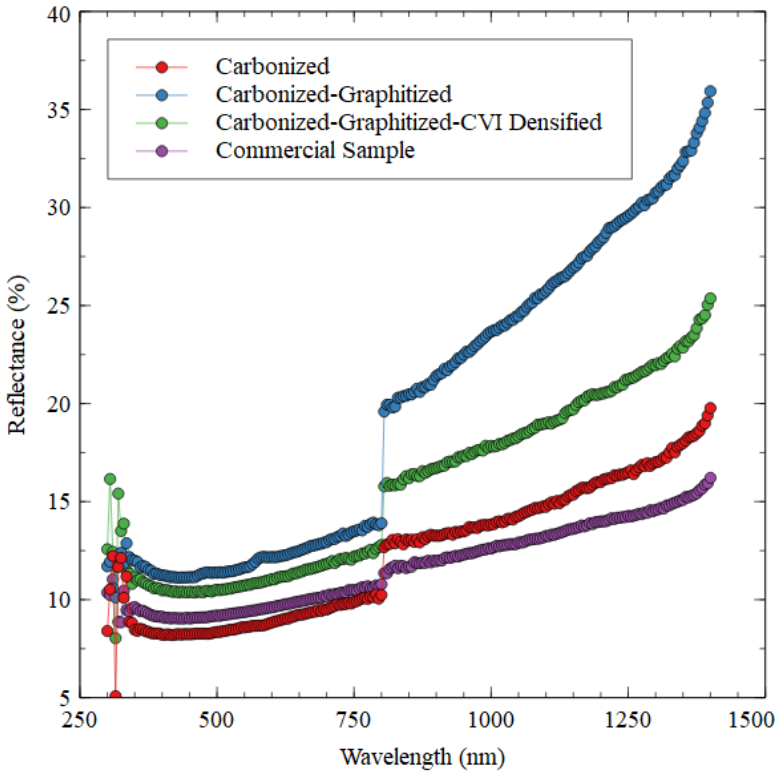

Figure 2.3 Spectral Reflectance of Unprotected Carbon Samples

Then, samples were measured with the required protective coating. This coating is described in chapter 2.1. Four samples are compared for this study and are summarized in Table 2.5. The goal of this study is to characterize the difference in optical properties between the uncured and cured coating and determine the quality of Pyromark coating for 1 and 2 coats.

Table 2.5 Protected Sample Descriptions for Optical Property Measurements

Specimen	Process
1	Protective Coated (Uncured)
2	Protective Coated (Cured)
3	Pyromark (1 Coat)
4	Pyromark (2 Coat)

The measured values for spectral reflectance were compiled into a comparative graph shown in Figure 2.4. The data shows that there is little difference in optical properties of the coating before and after curing. The coating also appears to reduce the reflectance of the composite compared to the unprotected samples. Furthermore, 1 Pyromark coat yields superior optical properties to 2 coats. Overall, the Pyromark coated samples have lower reflectance at the smaller wavelengths.

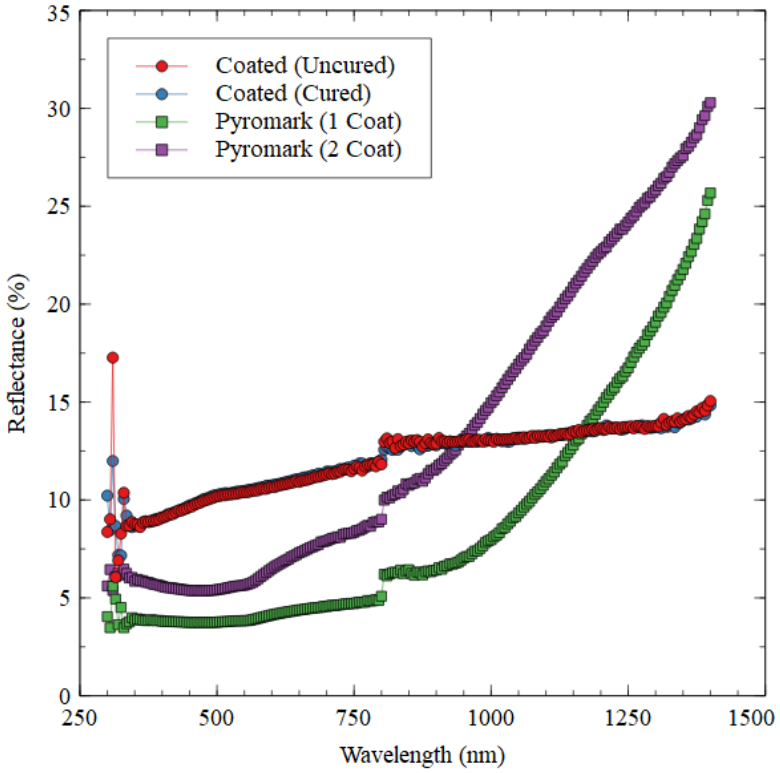

Figure 2.4 Spectral Reflectance of Protected Carbon Samples

The reflectance values were used alongside a numerical integration method to calculate the solar weighted absorptance of the different samples. These calculated values can be seen in Table 2.6. The values are also displayed in Figure 2.5 for ease of comparison. The absorptance of the unprotected specimens remains similar regardless of the stage of processing, the commercial sample exhibits a similar yet, slightly higher absorptance. The protected samples have nearly identical absorptance before and after the curing process and a single coat of Pyromark yields a greater absorptance than 2 coats. Unsurprisingly, the Pyromark coated samples have the greatest absorptance out of all the samples.

Table 2.6 Carbon-carbon Composite Solar Weighted Absorptance

Specimen Type	Solar Weighted Absorptance
1. Carbonized	.887
2. Carbonized – Graphitized	.825
3. Carbonized – Graphitized – CVI Densified	.857
4. Commercial Sample	.889
5. Coated (Uncured)	.882
6. Coated (Cured)	.882
7. Pyromark (1 Coat)	.931
8. Pyromark (2 Coat)	.890

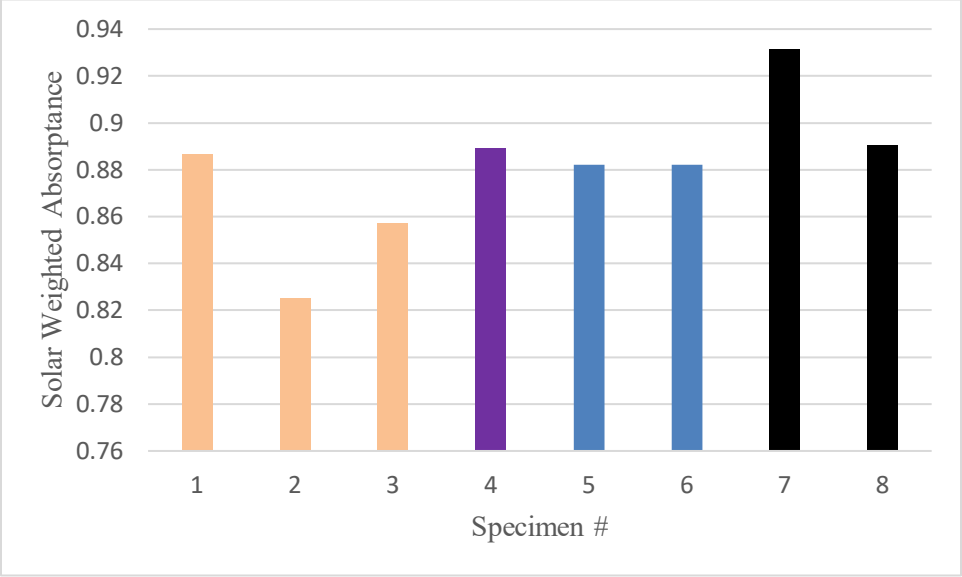

Figure 2.5 Specimen Solar Weighted Absorptance

2.3.2 Thermal Conductivity Analysis

Thermal conductivity values have been calculated for PAN-based and pitch-based fabricated samples and a commercial carbon/carbon composite from Across Composites. The PAN-based fibers exhibit thermal conductivity values below what is desired shown in Figure 2.6. Surprisingly, the graphitization step appears to have decreased the thermal conductivity of the sample.

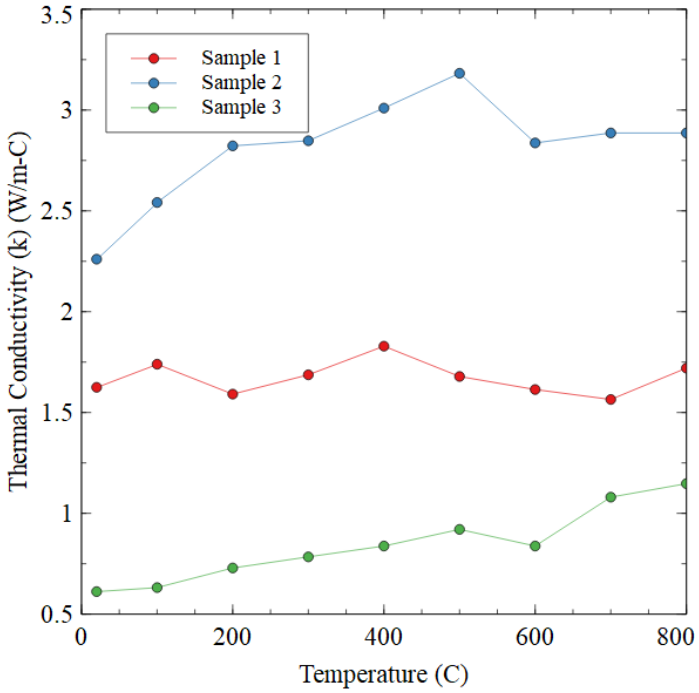

Figure 2.6 PAN-based Specimen Thermal Conductivity Values by Temperature

Ohlhorst was able to measure through plane thermal conductivities up to about 12 W/m-K, at the temperatures of interest, depending on the processing method [32]. Figure 2.7 shows that the composite processing method used in this study lies on the lower end of Ohlhorst's measured values. While the current measured values are lower than expected, commercial samples and cited work shows this level to be achievable with Ohlhorst's measured values up to 12 W/m-K and over 15 W/m-K observed by [33]. Across Composites advertised through-plane conductivity of about 15 W/m-K and measurements showed this was true. One explanation for the low thermal conductivity is the type of fibers used in the composite. The previously measured PAN-based samples performed below expectations so a composite made with pitch-based fibers was measured and found to have a through plane thermal conductivity of about 13 W/m-K.

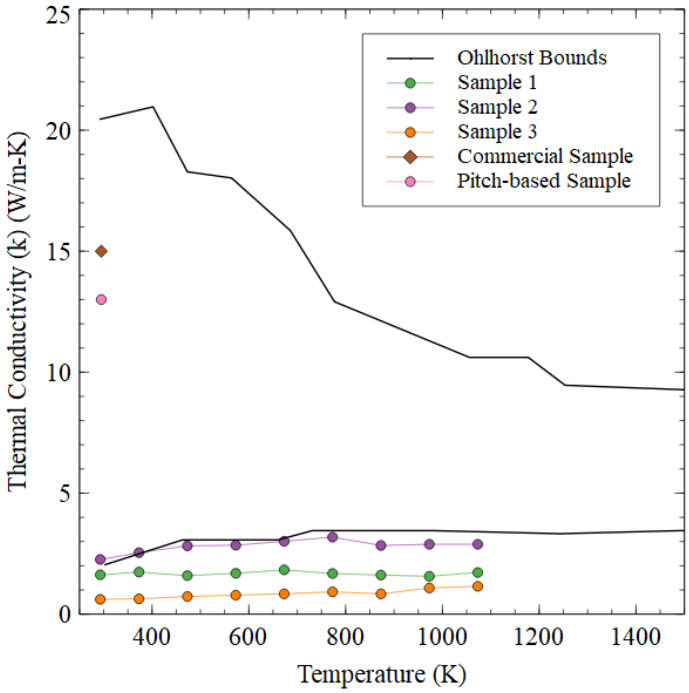

Figure 2.7 Carbon/carbon composite samples thermal conductivity compared to Ohlhorst's Measured Range

2.3.3 High Flux Solar Simulator Aging Analysis

UV aging was conducted via high flux solar simulator. A representative temperature profile is shown in Figure 2.8 for 20 cycles. Note that there is a transient response at the beginning cycles due to the temperature of the composite and the temperature of the platform that the composite rests on.

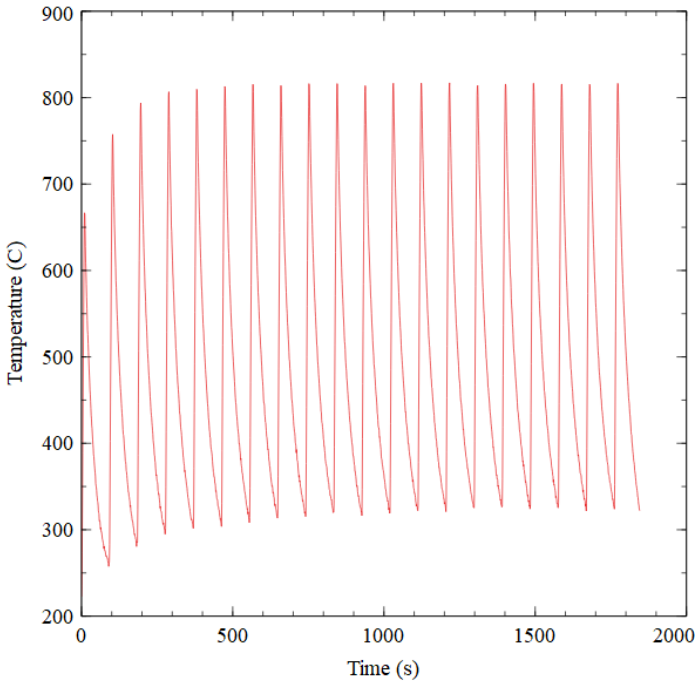

Figure 2.8 Composite Temperatures Over 20 Cycles on HFSS

The optical properties of the composite were measured and recorded. At high temperatures, an oxide layer forms that is white in color, reducing the absorbing capabilities of the composite. Figure 2.9 shows the spectral reflectance profiles at 0, 90, 190, and 290 cycles visualizing the formation of the oxides. It is shown that the oxide layer changes the shape of the spectral reflectance profile and then translates upwards as more oxides form.

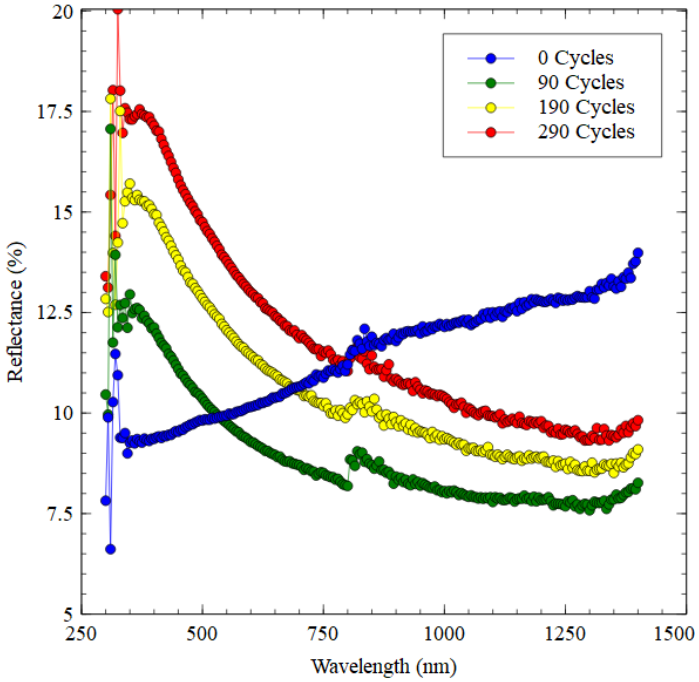

Figure 2.9 Spectral Reflectance Changes with Cycles

The reflectance profiles were then used to calculate the solar weighted absorptance at each cycling interval shown in Figure 2.10. As expected, the solar weighted absorptance of the composite decreases as more cycles occur and more oxides are formed. There is a significant jump in solar weighted absorptance during the first 10 to 20 cycles, this is due to the conditioning of the SiC coating on the composite and is not related to the formation of oxides. The solar weighted absorptance trends downward and it is expected that an asymptote could be reached after a large number of cycles.

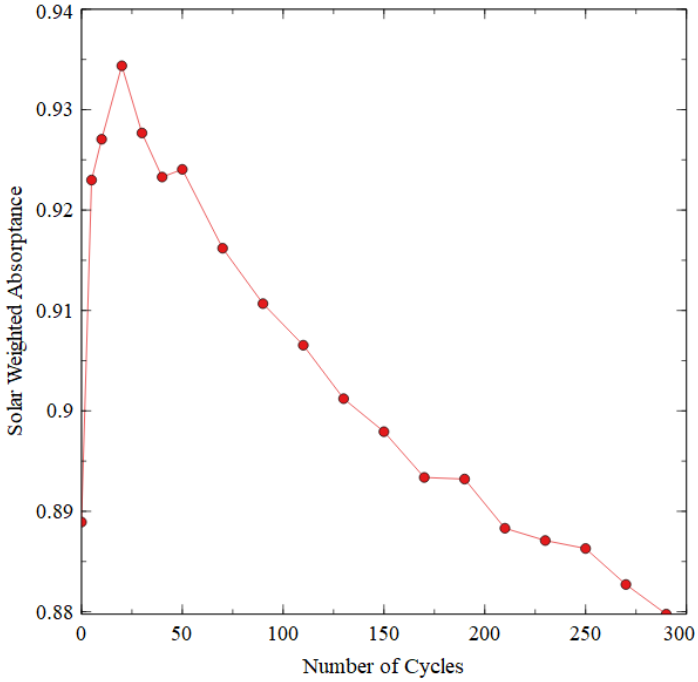

Figure 2.10 Solar Weighted Absorptance Changes with Cycle Number

Finally, the mass change was characterized for the carbon/carbon composite and is shown in Figure 2.11. A consistent mass gain is observed which could represent a self-healing quality of the coating. Again, it appears that an asymptote could be reached with a large enough number of cycles.

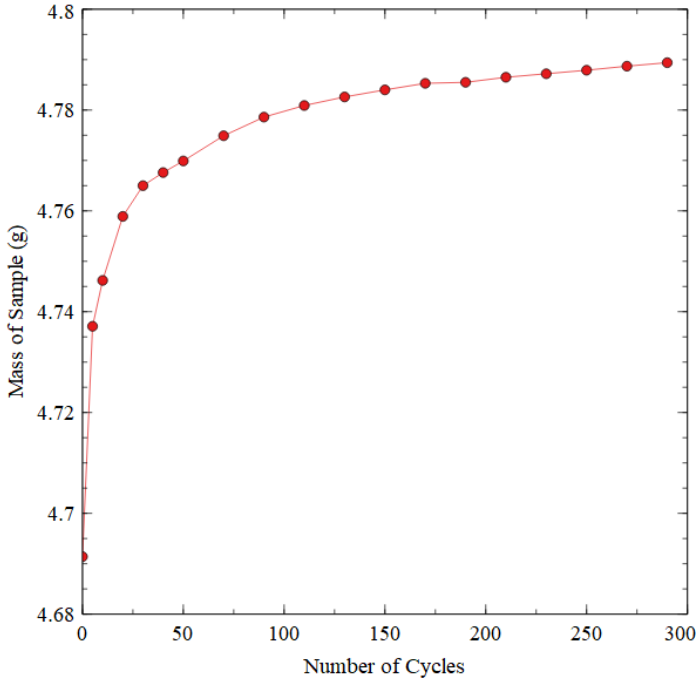

Figure 2.11 Sample Mass vs. Number of Cycles

2.3.4 Isothermal Tube Furnace Aging Analysis

Samples were aged in the tube furnace at 850 °C for 100-hour intervals. It was found that the stability of the current coating is of concern when held at constant temperature. Out of 10 samples, 6 survived the first 100 hours of isothermal aging and none survived up to 200 hours of aging. This is likely due to the oxide formation and conditioning of the coating. In order for the coating to reach its most resilient state, it must be heated to temperatures above 1000 °C. Thus, since the aging was conducted at 850 °C, the coating was unable to be conditioned properly to survive long stints at high temperature. Furthermore, the samples that did survive show the necessity for a solar selective coating such as Pyromark. Figure 2.12 shows the solar weighted absorptance of both uncoated and Pyromark coated samples that survived the first 100 hours of aging.

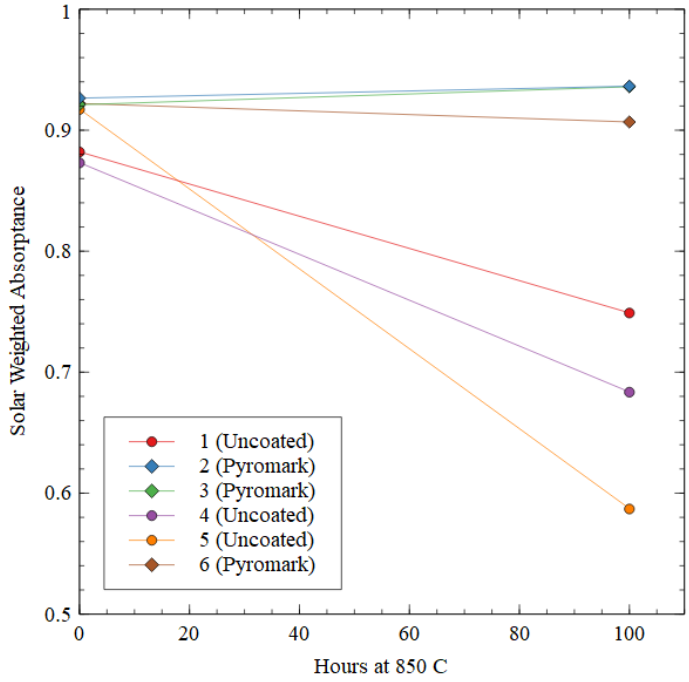

Figure 2.12 Solar Weighted Absorptance vs. Hours at 850 C

The mass change was characterized for all samples and most samples exhibited mass loss for the 100 hours of aging shown in Figure 2.13. This is of concern since a mass gain is expected with the large amount of oxides that form on the sample. Furthermore, the samples that have a mass reduction down to 1 to 2 grams lit on fire and only the SiC coating was left. This represents a concern for this coating and a reliable method to stabilize the coating is necessary.

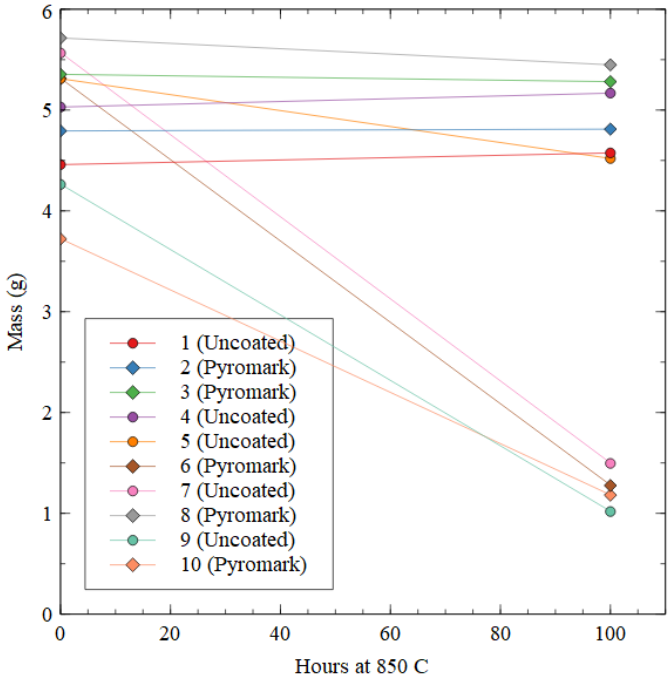

Figure 2.13 Sample Mass vs. Hours at 850 C

CHAPTER THREE: RECEIVER MODELING

3.1 Single Plate Analysis Methodology

A full-scale receiver of this nature would be constructed out of many small single plate modules. Therefore, it is important to understand the operation and design space for the single plate module before looking at the bigger picture.

3.1.1 Numerical Model

This study uses a carbon/carbon composite microvascular plate, a small section of the full-scale receiver design. The plate has an inlet, outlet, and some connecting path in between to maximize efficiency of heat transfer. The surface of the receiver is receiving and dissipating energy through radiation, convection, and conduction. The radiant energy from the sun is absorbed at the surface, the surface emits energy to the environment through both radiation and convection, and energy is conducted into the material. boundary conditions used for this study can be seen in Figure 3.1.

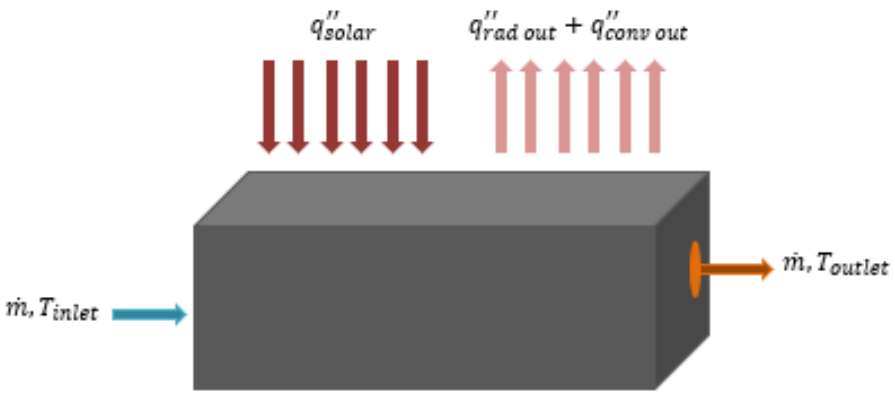

Figure 3.1 Single Plate Module Boundary Conditions

ANSYS computational fluid dynamics (CFD) package Fluent was used to run simulations based around the numerical model. Modelling and meshing of the 3-

dimensional receiver plates were done using ANSYS Space Claim and Mechanical respectively. Mesh sizing was adjusted to be finer in and near the channels of the receiver and coarser toward the edges of the receiver to improve computing time. An example mesh is shown in Figure 3.2.

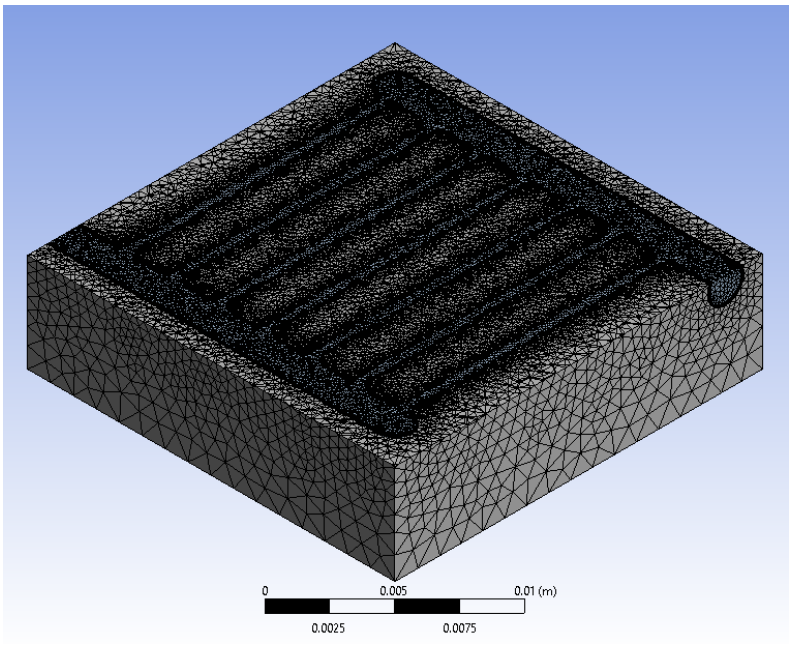

Figure 3.2 Single Plate Mesh Sizing Example

Due to the limitations of ANSYS Fluent, a user defined function (UDF) was implemented to include simultaneous radiation, convection, and conduction at the surface of the receiver. The transfer of energy at the surface is broken into solar radiation in, ambient radiation in, convection in, radiation out, and convection out. Conduction at the surface is not described in the UDF since Fluent is capable of handling this. The previously mentioned parts of energy transfer at the surface are described using Eq. (3.1-3.5).

$$q''_{solar\ in} = aq''_{solar} \tag{3.1}$$

$$q''_{rad\ in} = \varepsilon\sigma T^4_{ambient} \tag{3.2}$$

$$q''_{rad\ out} = \varepsilon\sigma T^4_{surface} \tag{3.3}$$

$$q''_{conv} = h(T_{surface} - T_{ambient}) \tag{3.4}$$

Where $q''_{solar\ in}$ is the solar radiation absorbed by the receiver, a is the absorptivity, q''_{solar} is the concentration of solar flux, $q''_{rad\ in}$ is the radiation into the receiver by the surroundings, ε is the emissivity, σ is the Stefan Boltzmann constant, $T_{ambient}$ is the ambient temperature around the receiver, $q''_{conv\ in}$ is the convective heat transfer into the receiver, h is the heat transfer coefficient between the air and receiver, $q''_{rad\ out}$ is the radiation from the receiver to the surroundings, $T_{surface}$ is the surface temperature of the receiver, and $q''_{conv\ out}$ is the convective heat transfer from the receiver to the surrounding air.

The total heat flux at the surface can then be simply calculated as is shown in Eq. (3.6).

$$q''_{total} = q''_{solar\ in} + q''_{rad\ in} - q''_{rad\ out} - q''_{conv} \tag{3.6}$$

Where q''_{total} is the totality of the heat flux incident at the surface of the receiver.

ANSYS Fluent allows for many facets of customization in CFD simulation. For this study, the important models to consider are the energy model and the viscous model. The energy model must be set to on in order to handle the thermal profile of the system. The viscous model has many options and becomes important since the fluid flow is turbulent within the channels. This study utilizes the shear stress transport (SST) k-omega viscous model as this model is directly usable all the way down to the pipe wall through

the viscous sub-layer. This is especially important when dealing with microchannels where a large amount of the simulation needs to consider near-wall scenarios.

Convergence of the simulations in this study is characterized by either a flat residual line after 2000 iterations or an energy residual below 1e-08. It was found that values calculated by the simulation differ minimally in both of these situations.

3.1.2 Pathway Design

The channels of the plate are designed similarly to a billboard design with large diameter (2 mm) headers at the inlet and outlet and smaller diameter (1mm) connecting channels between the headers. Examples of this channel structure can be seen in Figure 3.3.

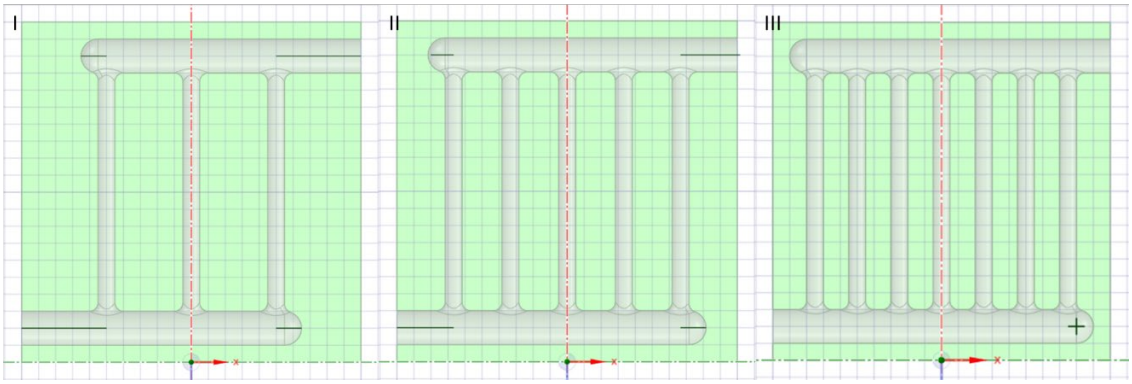

Figure 3.3 Single Plate Channel Structure for 3-path (Left), 5-path (Middle), and 7-path (Right) Design

To determine the optimal number of connecting paths, a series of simulations were conducted parameterizing the number of paths. Simulations included 3, 5, 7, and 9 connecting paths with liquid sodium as the working fluid at 750 kW/m^2 irradiance. The mass flow rate is difficult to compare when the number of connecting paths is changing because, for the same inlet mass flow rate, the connecting channels will have greater mass flow with less paths than they will with more paths. Therefore, the pressure drop

was matched between the designs instead. These parameters are shown in Table 3.1. The results of these simulations are compared by the thermal efficiency and the maximum surface temperature. Designs with higher thermal efficiency and lower surface temperatures are favored.

Table 3.1 Simulation Parameters for Path Number Comparison

Parameter	Value
# of connecting channels	3, 5, 7, 9
HTF	Liquid sodium
Irradiance (kW/m^2)	750
Pressure drop (psi)	5

The thermal efficiency for the single plate receiver can be calculated as an energy balance of heat energy incident on the surface of the receiver versus the heat absorbed by the HTF. Eq. (3.7) shows this relationship.

$$\eta_{th} = \frac{\dot{m} C_p \Delta T}{GA} \tag{3.7}$$

Where η_{th} is the thermal efficiency of the single plate receiver, $\dot{m}$ is the mass flow rate at the inlet, C_p is the specific heat of the HTF, ΔT is the change in temperature of the HTF from the inlet to the outlet, G is the concentration of solar flux incident on the receiver, and A is the receiving area of solar flux.

3.1.3 Receiver Design Constraints

Design for the single plate modules is limited by the allowable pressure drop and allowable strain. The pressure drop for the single plate module is limited to 5 psi and is imposed by the Department of Energy (DOE). This constraint is in place since the full-scale system would consist of many single plate modules in serial chains. If the pressure drop for a single module were excessively high, the pump work required for a full-scale receiver would negatively affect the performance of the overall plant performance.

The carbon/carbon composite is similar to other composites in that it is strain limited [34]. Thus, the allowable strain for the composite is limited at .2%. Because the composite thermal loading outweighs any mechanically induced strain, Eq. (3.8) is used as a conservative way to estimate strain in the single plate module.

$$E = \alpha_{CTE}\Delta T \tag{3.8}$$

Where E is the strain, α_{CTE} is the coefficient of thermal expansion (CTE), and ΔT is the difference between the HTF inlet temperature and the maximum temperature of the single plate module.

This method is conservative since the minimum temperature of the composite is hotter than the inlet temperature of the HTF.

3.1.4 Heat Transfer Fluids

This study utilizes supercritical CO_2 (sCO_2), liquid Na, and KCl-$MgCl_2$ as a gas, molten metal, and molten salt respectively. The different types of HTF allow for comparison between the different couplings of HTF and receiver. sCO_2 is treated slightly differently from the other HTFs due to the differences in material properties. While liquid Na and KCl-$MgCl_2$ have somewhat comparable densities, sCO_2 is about a magnitude less dense. Because of this difference in density coupled with the fact that a receiver power output is somewhat tied to the mass flow rate of the HTF, sCO_2 must run beyond the pressure drop constraint of 5 psi mentioned in 3.1.3. The material properties of the HTFs used in the CFD simulations are shown in Table 3.2 [25], [35], [36]. The properties used are constant due to the limitations of the CFD solver however, this also reduces computational cost of the simulation. The properties are assuming the HTF is at 900 K.

Table 3.2 HTF Thermophysical Properties Used in Simulation

Material	Density (kg/m^3)	Cp (J/kg-K)	Viscosity (kg/m-s)	Thermal Conductivity (W/m-K)
sCO_2	49.31	1247	4.31×10^{-5}	0.094
Na	801.7	1257.52	2.04×10^{-4}	62.5
KCl-$MgCl_2$	1557.04	1010.21	3.46×10^{-3}	.442

3.1.5 Carbon/carbon Composite Properties

The carbon/carbon composite properties are shown in Table 3.3 [32], [37]. The composite is simulated under the assumption that there is a solar selective coating such as Pyromark 2500 S [38]. The through-plane thermal conductivity of the composite is assumed to be within a range of 3-12 W/m-K as the value can vary even if specimens undergo similar processing [32]. This range could be considered conservative as advancements in the materials fields have generated composites with through-plane thermal conductivities over 15 W/m-K [33]. The coefficient of thermal expansion has 2 values, the lower is the actual value for the composite, and the higher value is a near 1.5 times factor of safety value used for the strain constraint calculations.

Table 3.3 Carbon/carbon Composite Properties Used in Simulation

Property	Value
Density (kg/m^3)	1700
C_p (J/kg/K)	1800
In-plane Thermal Conductivity (W/m-K)	25
Through-plane Thermal Conductivity (W/m-K)	3-12
Coefficient of Thermal Expansion (K^{-1})	4×10^{-6}, 5.75×10^{-6}
Absorptivity	.94
Emissivity	.88

3.1.6 Simulation Parameterization

Parameterized simulations were used to establish a design space for the carbon/carbon composite and HTF pairings. The inlet temperature of the HTF, through-

plane thermal conductivity of the carbon/carbon composite, solar flux level, and number of connecting channels are parameterized to generate the design spaces. These spaces are readily comparable to more easily understand trends in the single plate system. Simulations were conducted with equivalent allowable pressure drop disregarding sCO_2 (see 3.1.4). Table 3.4 shows parameterized variable values.

Table 3.4 Parameterized Values Used in Simulation

Parameter	Value
Inlet Temperature (K)	473-1073 K
Through-plane Thermal Conductivity (W/m-K)	3-12
Solar Flux (kW/m^2)	500, 750
Number of Connecting Channels	5, 7

The 3 goals of the parameterized simulations are to visualize the different performances of the 3 HTFs, compare operational performance of the receiver at different flux levels, and compare performance with different numbers of connecting channels. The performance of the receiver can be described in different ways, all of which can be useful. The thermal efficiency is valuable as the efficiency of the receiver has a great impact on the overall plant efficiency. The surface temperature of the receiver is important to minimize as radiative losses become paramount at high temperatures. Furthermore, a higher maximum temperature leads to a greater induced thermal strain which compromises the integrity of the design.

3.2 Single Plate Analysis Results

3.2.1 Pathway Results

The single plate receiver module was parametrically simulated with varying number of connecting paths. The optimal number of paths for this study was found to be 7 as this point represents both the highest thermal efficiency and lowest maximum

surface temperature although by a small margin. The results from this study are shown in Figure 3.4. The most likely explanation for the decreasing performance after 7 connecting channels is the pressure drop constraint. Adding more connecting channels increases pressure drop for the same mass flow rate and it appears that the mass flow rate is not high enough to support more than 7 connecting channels effectively. These results show that the thermal efficiency is only mildly affected by the number of connecting channels while the maximum surface temperature appears more sensitive to these changes. Therefore, the single plate receiver geometry could represent an effective pathway to more resilient receiver design due to the limitations caused by the thermomechanical strain.

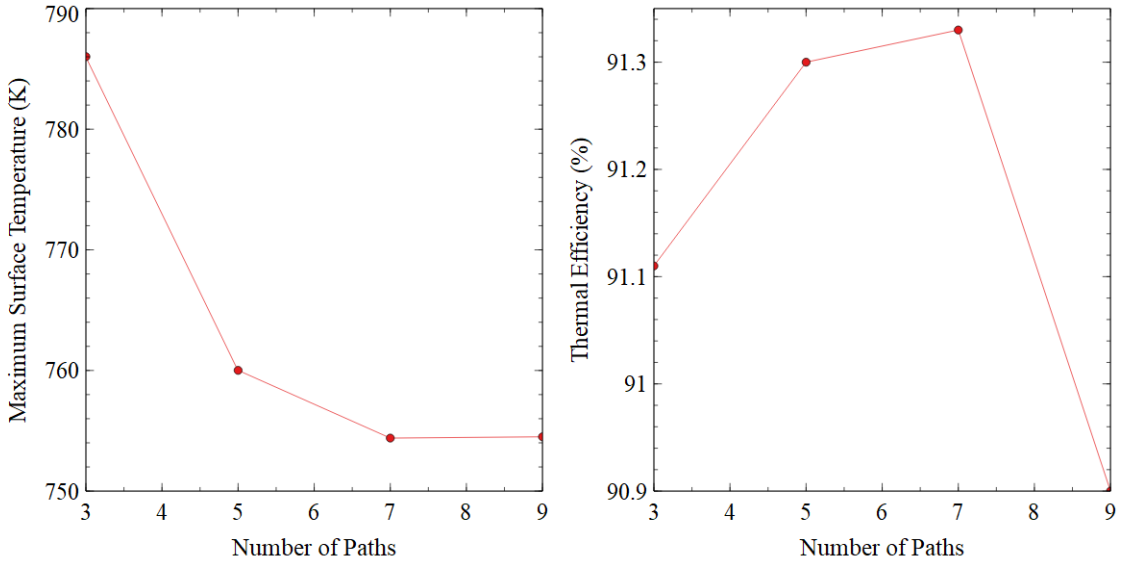

Figure 3.4 Maximum Surface Temperature Vs. Number of Connecting Channels (Left) and Thermal Efficiency Vs. Number of Connecting Channels (Right)

3.2.2 Parametric Single Plate Performance

The thermal results have been compiled into contours to easily visualize receiver performance. Each contour has 2 additional dashed lines. These lines are representative of a strain limit of 0.2% which is considered failure for the composite. The upper and

lower lines represent factors of safety of 1.5 and 1 respectively. Strain is used as a general way of predicting failure in this case because composites are typically strain limited [34]. Data that lies below the curves are considered failing designs as they would not be capable of handling the strain induced by the thermal gradient. Figure 3.5 shows the thermal results for sCO_2. This batch of simulations is slightly different from the others as the pressure drop was not restrained to 5 psi. This was done because, as a gas, sCO_2 must be pumped at a much higher velocity to mimic the mass flow rate of the other HTF's. sCO_2 has a maximum efficiency of about 90.7% on this contour. It is important to note how influential the carbon/carbon composite thermal conductivity is with regards to the thermal gradient at low inlet temperatures. At an inlet temperature of 473 K, there is a difference in maximum surface temperature caused by thermal conductivity of about 524 K.

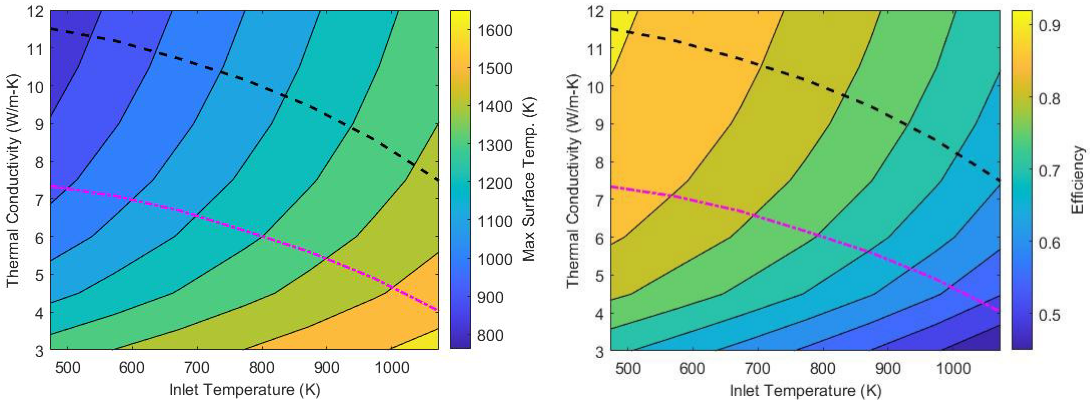

Figure 3.5 sCO_2 Contours for Surface Temperature as a Function of Inlet Temperature and Thermal Conductivity (Left) and Thermal Efficiency as a Function of Inlet Temperature and Thermal Conductivity (Right)

Liquid sodium shows promise in its high thermal conductivity and overall ability to receive heat energy from the solar receiver. Figure 3.6 shows that liquid sodium has an impressive operating window above the 1.5 factor of safety line. The minimum thermal

conductivity required to use the 473 K inlet temperature is about 9.66 W/m-K. At this minimum value, the receiver could see thermal efficiency of about 91%. If the 12 W/m-K conductivity value was achieved, this efficiency could reach 91.89%. Overall, simulations indicate that liquid sodium performs very well with the lowest surface temperatures and highest thermal efficiencies of the 3 HTF's. The figure also shows the importance of minimizing radiative losses, represented by the lower surface temperatures. Radiative losses tend to outweigh convective losses when exceptionally high temperatures are reached.

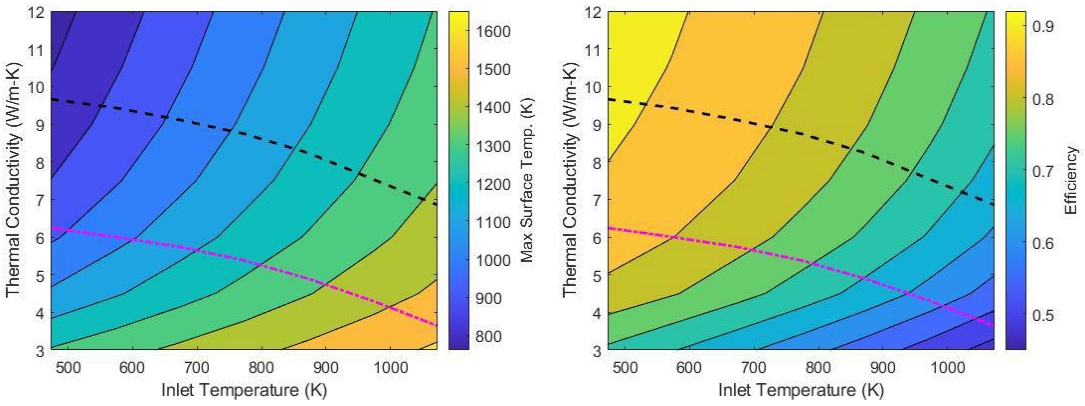

Figure 3.6 Liquid Na Contours for Surface Temperature as a Function of Inlet Temperature and Thermal Conductivity (Left) and Thermal Efficiency as a Function of Inlet Temperature and Thermal Conductivity (Right)

Some of the most recurrent HTF's used in receivers today are molten salts. In this case, KCl-$MgCl_2$ is the salt of choice. This salt has been characterized and defined as a quality HTF for solar thermal receivers [25]. Figure 3.7 shows the thermal results from the molten salt batch simulations. The maximum achievable efficiency over the 1.5 factor of safety is about 90%. This design option happens at 12 W/m-K thermal conductivity and just a touch above 473 K inlet temperature since the design point at 473 K is below the constraint. These design options can all be expanded significantly with a receiver

geometry that increases heat transfer between the carbon/carbon composite and HTF. Decreasing the maximum surface temperatures by even 10 K would increase the area of possibilities enough to see higher efficiencies.

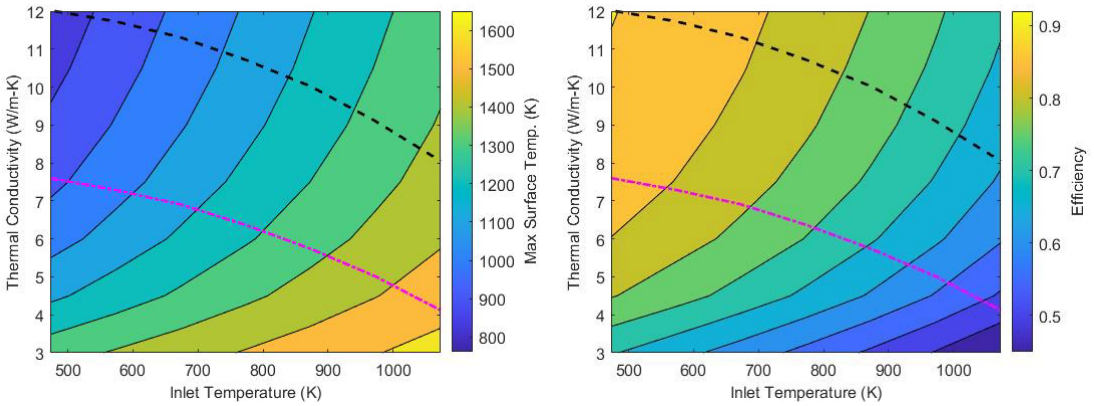

Figure 3.7 KCl-$MgCl_2$ Contours for Surface Temperature as a Function of Inlet Temperature and Thermal Conductivity (Left) and Thermal Efficiency as a Function of Inlet Temperature and Thermal Conductivity (Right)

Figure 3.8 shows the results of the 7-path receiver operating at 500 kW/m^2 with molten salt as the HTF at the same mass flow rate as the 750 kW/m^2 simulations. The performance of the simulation is both exactly what is expected and slightly misleading. At face value, it looks like the receiver runs better at lower irradiance due to the slightly increased efficiency. However, while thermal efficiency is a good measure of performance, it must be noted that the outlet temperature is significantly lower with the reduced solar flux value. To match the outlet temperature of the higher flux levels, mass flow rate in the channels would have to be reduced. Whether the mass flow rate is reduced to match outlet temperatures or not, the power output will be lower with a lesser irradiance. The efficiency likely runs higher since radiation losses dominate thermal performance. When the receiver is run at a lower solar flux, the surface remains at a

much lower temperature leading to reduced radiative losses. This is shown both by the surface temperature contour as well as the lowered restraint lines.

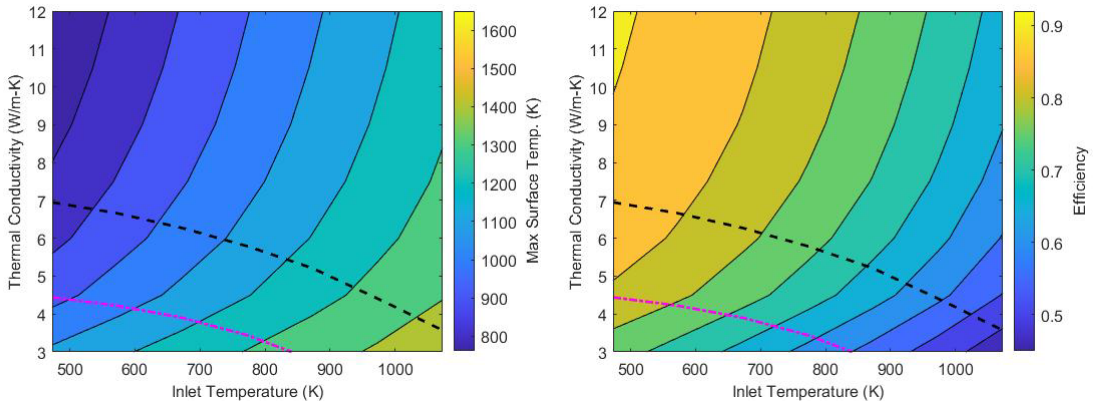

Figure 3.8 Comparative Contours with Molten Salt Running at 500 kW/m^2 Rather Than 750 kW/m^2

Figure 3.9 shows the performance of a 5-path variant of the receiver operating under 750 kW/m^2 with molten salt as the HTF. As is expected, the thermal gradient is worsened by the decreased number of paths. The restraint lines have increased significantly from the 7-path design and the efficiency has decreased slightly. This is further evidence that increasing path number is beneficial to the integrity of the receiver. It is also important to note the change in maximum efficiency is less than a percent, based on this, paths are mostly beneficial to distribution of heat at this level and not thermal efficiency.

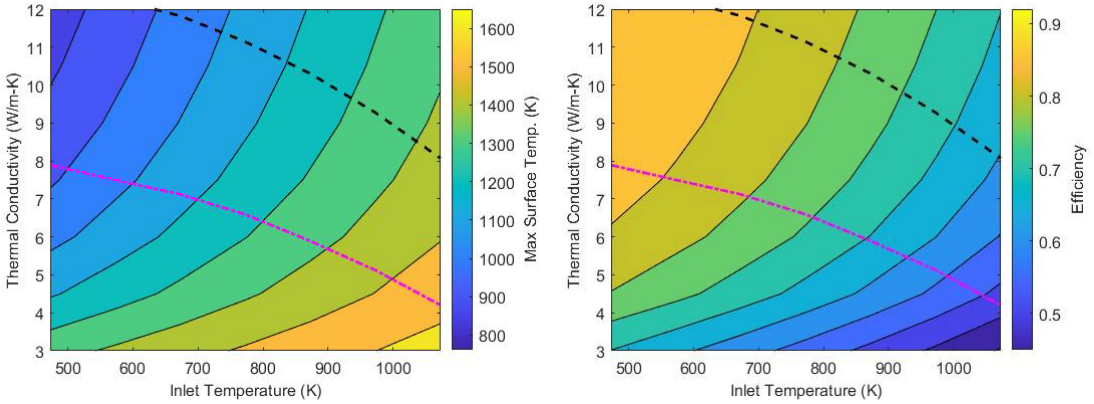

Figure 3.9 Comparative Contours for a 5-path Receiver with KCl-$MgCl_2$ Rather Than a 7-path Receiver

Table 3.5 shows the summarized results of the parametric simulations. Depending on the HTF, irradiance, and number of connecting paths, the parameterized options have different break points to reach a 1.5 factor of safety. Note that the values listed in the table are the most difficult to achieve values as far as composite processing and thermal strain on the receiver.

Table 3.5 Parametric Simulation Breakpoints for 1.5 Factor of Safety

HTF	Irradiance (kW/m^2)	# Paths	Factor of Safety	Thermal Conductivity (W/m-K)	Inlet Temperature (K)
sCO_2	750	7	1.5	11.5	473
Liquid Na	750	7	1.5	9.7	473
KCl-$MgCl_2$	750	7	1.5	12	480
KCl-$MgCl_2$	500	7	1.5	7	473
KCl-$MgCl_2$	750	5	1.5	12	633

3.3 Full-scale Receiver Methodology

3.3.1 Full-scale Design Point

Following the single plate analysis, a full-scale receiver composed of many single plates in series and parallel is designed and analyzed. The single plate receivers are put in serial chains of 15 and then stacked in a parallel manner. Then, the parallel chains are fed

by main channels on the full-scale module in order to greatly reduce the number of connections. Figure 3.10 describes how the full-scale receiver modules are designed.

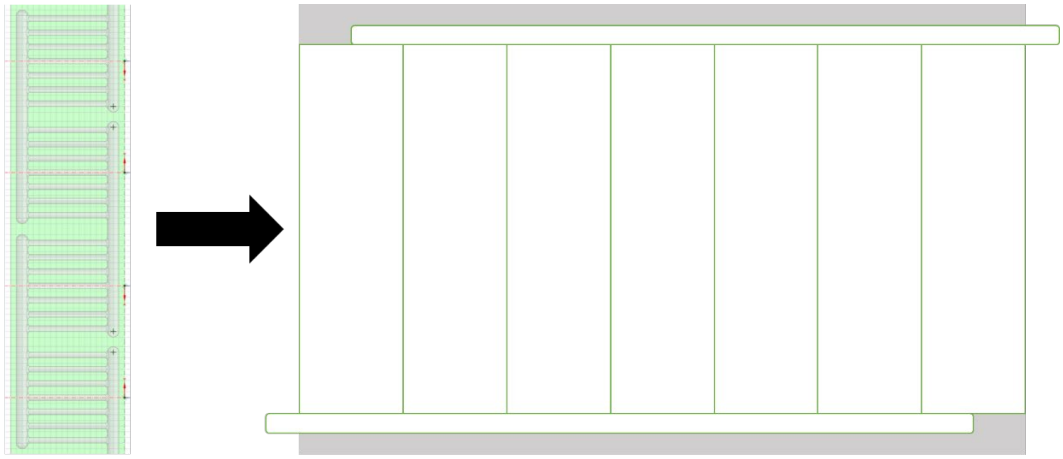

Figure 3.10 Full-scale Receiver Module Made of Single-plate Receivers

The full-scale receiver modules can then be numbered up in order to create a full-scale receiver design. The design generated in this study is a cylindrical receiver with a base radius of 8 m and a height of 12 m. The full-scale receiver is illustrated in Figure 3.11.

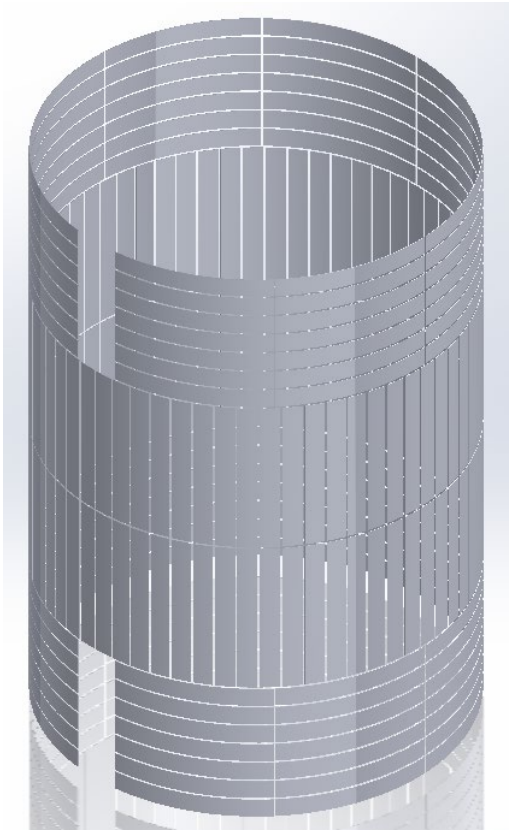

Figure 3.11 Full-scale Cylindrical Receiver Design

Then, the full-scale design is analyzed considering a specific design point, an approach typically employed in the early-stage receiver design phase [39]–[41]. The selected design point for the analysis is at solar noon on the summer solstice. The hypothetical plant using this newly presented receiver is assumed to be located in Seville (37.56° N, 5.33° W), resulting in a DNI of 991 W/m^2 at that time and location during clear-sky conditions. The receiver is studied as part of a plant with a heliostat field layout like the one in Gemasolar [42], [43], constituted by 2650 heliostats of an effective mirror area of 115.7 m^2 each. Thus, the heat flux distribution analyzed is presented in Figure 3.12, relying on a nearly-equatorial aiming strategy.

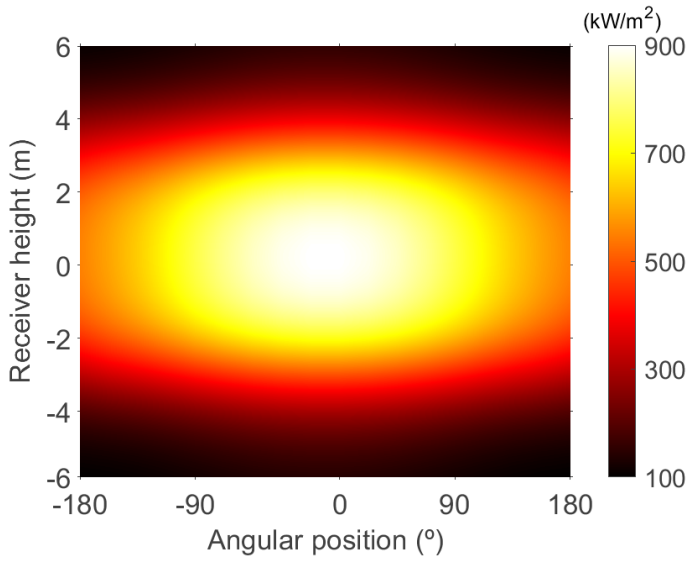

Figure 3.12 Cylindrical Flux Map Design Point

To avoid excessive computational cost that a full-scale model would incur, the utilized simulation method is summarized in Figure 13. For a given flux level, the single plate receiver is simulated with modified mass flow rates that allow for the desired outlet temperature. In doing this, all largescale panels will have the same outlet temperature regardless of flux level. This process is repeated for each flux level at intervals of 100 kW/m^2.

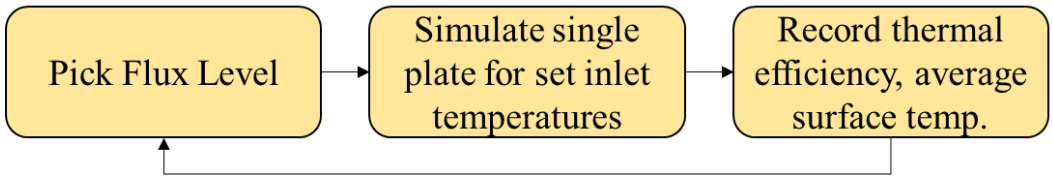

Figure 3.13 Full-scale Simulation Flow-chart

3.3.2 Mass Flow Rate

The flux profile imposed on a full-scale receiver yields areas of the receiver at different flux levels. To have a similar output temperature for each of the full-scale modules, the mass flow rate must be reduced in areas of lower flux and vice versa to

allow for the proper amount of heat transfer from the walls of the module to the HTF. To find the proper mass flow rate a flux level was chosen, for that flux level a series of simulations were conducted across a range of inlet mass flow rates to find the particular flow rate that would give the desired outlet temperature. The inlet and outlet temperatures used for the full-scale simulations are based on the desired temperature range for next generation receivers of 520°C to 720°C [44].

3.3.3 Average Surface Temperature

Characterizing the average surface temperatures of the simulated full-scale receiver is an exercise to better understand the conditions that the carbon/carbon composite could be facing during operation. First, the single plate receiver modules are simulated for individual average surface temperatures relative to the given inlet temperature that would be experienced in a serial chain. The average temperatures for the single plate receivers are then averaged again to give the average surface temperature for a serial chain of single plate modules at the given flux level. Finally, due to the symmetry of the full-scale receiver modules, the average surface temperature of the full-scale module can be assumed to be the same as that of the serial chain of single plate modules.

3.4 Full-scale Receiver Results

3.4.1 Simulated Full-scale Performance

The full-scale receiver performance is summarized in Table 3.6. This design achieves a thermal efficiency of 85.04% with an estimated power output of 439 MW. However, with the design point flux map and desired outlet temperature, 112 of the panels would not be in use due to the low flux levels (0-400 kW/m^2) not allowing for turbulent flow in the channels. In order to reach the desired outlet temperature at 400

kW/m^2, the molten salt inlet velocity would be low enough that the Reynolds number is below 2000. This was verified by running a simulation with the incident flux set to 400 kW/m^2 and the Reynolds number at the inlet set to 2000. The outlet temperature for this simulation was less than the desired outlet temperature. Potentially, the desired outlet temperature for the system could be reduced, allowing for the use of these panels at the given design point, although this is not explored in this work. These panels would likely still be in use at different times of day or with a more homogeneous aiming strategy.

Table 3.6 Summary of Full-scale Receiver Performance

Metric	Value
# of Modules (in use)	126
Total Mass Flow Rate (kg/s)	2.123
Average HTF ΔT (K)	204.875
Overall Efficiency (%)	85.04
Estimated Power Out (MW)	439

3.4.2 Average Surface Temperature Results

Figure 3.14 shows approximate values for the receiver surface temperatures. These values are based on average surface temperatures of the panels depending on the average incident surface flux. It is shown that the average surface temperatures could reach as high as 1243 K in the 900 kW/m^2 flux zones. With surface temperatures as high as these, refining the path geometry or increasing the allowable pressure drop could significantly improve the resiliency of the full-scale system.

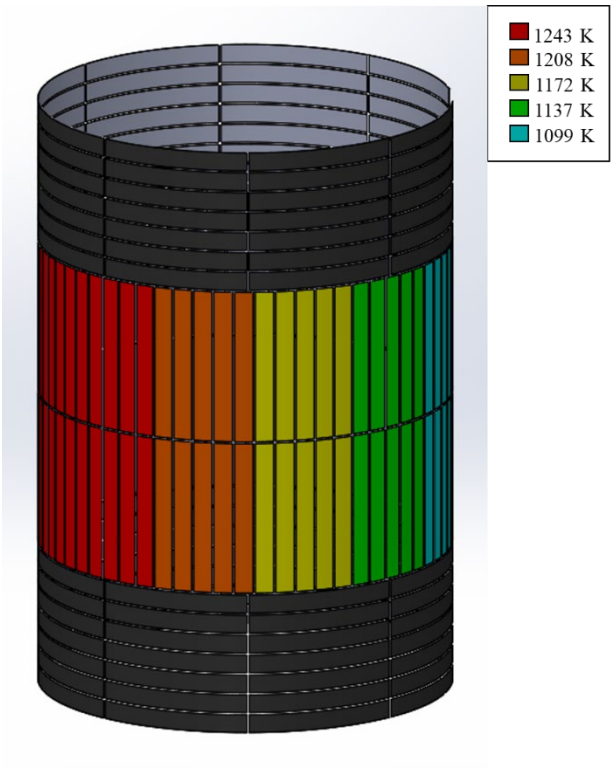

Figure 3.14 Full-scale Receiver Average Surface Temperature Visual

CHAPTER FOUR: CONCLUSION

This study investigates the potential for a new carbon/carbon composite for solar thermal receiver applications capable of withstanding greater thermal loads than current metallic receivers. The composite was characterized, experimentally aged, and then modelled via ANSYS Fluent in a variety of conditions to generate a design space for a nominal carbon/carbon composite receiver.

Characterization experiments show that a solar selective coating would be important for the composite. A single coat of Pyromark was found to yield a higher absorptivity and more stable coating. Thermal conductivity results show the composites made with PAN-based fibers are less thermally conductive than expected. A commercial sample and other publications show it is reasonable to expect a composite with through plane conductivity at or above 12 W/m-K. A fabricated pitch-based fiber composite further reinforced this notion measuring a through plane conductivity of about 13 W/m-K.

Cyclic aging was conducted via high flux solar simulator and the composite showed consistent mass gain potentially hinting at self-healing capabilities. The oxides forming on the composite that allow for mass gain also tend to change the shape of the spectral reflectance graph and decrease the solar weighted absorptance. Isothermal aging was more problematic for the carbon/carbon composite as only 6 of 10 samples survived the first 100 hours at 850 °C and no samples survived 200 hours. It was found that the oxides still formed but not enough to prevent burning of the composite. The amount of oxides formed significantly decreased the solar weighted absorptance from around 90%

to anywhere from 80 to 60% on uncoated samples. Pyromark coated samples maintained solar weighted absorptance of 90% or higher for at least the first 100 hours.

A single plate system was modelled for the nominal carbon/carbon composite receiver. Results show that decreasing inlet temperature and increased thermal conductivity of the composite allows for greater thermal efficiency at the cost of a higher thermal gradient. The effects of this gradient can be offset by the low CTE of the carbon/carbon composite and improvements in processing leading to greater thermal conductivity.

A full-scale model was created based on a design point for a cylindrical receiver. An advantage of using the modular elements is the customization of HTF flow rates for different flux gradients. A drawback to the design is the relatively large number of connections to each of the individual modules and the fact that not all modules were in use for the given design point. One way to avoid this could be the use of less equatorial aiming strategies for the heliostat field. This would homogenize the flux allowing for higher flux values on the edges of the receiver. A trade-off of this strategy would be increased spillage losses.

CHAPTER FIVE: FUTURE WORK

Future work for this study involves further cycling of the composite under the solar simulator until a steady state is reached regarding the solar weighted absorptance and mass changes. Cyclic aging of a Pyromark coated sample would also be beneficial to see how the UV aging may affect the solar selective properties of the coating. Furthermore, an experimental test setup consisting of a carbon/carbon composite specimen being on sun with a heat transfer fluid running through it would be desirable for validating simulation results.

Creating more refined methods for conditioning the coating to allow for better survival rates in isothermal aging would be helpful to better understand the lifetime for both the uncoated composite and one with Pyromark.

Finally, work is ongoing to refine the coating and make it both more resilient to high temperatures and maintain more favorable optical properties.

REFERENCES

[1] E. Kabir, P. Kumar, S. Kumar, A. A. Adelodun, and K. H. Kim, "Solar energy: Potential and future prospects," *Renewable and Sustainable Energy Reviews*, vol. 82, pp. 894–900, Feb. 2018, doi: 10.1016/J.RSER.2017.09.094.

[2] R. IRAM, M. K. ANSER, R. U. AWAN, A. ALI, Q. ABBAS, and I. S. CHAUDHRY, "PRIORITIZATION OF RENEWABLE SOLAR ENERGY TO PREVENT ENERGY INSECURITY: AN INTEGRATED ROLE," *The Singapore Economic Review*, vol. 66, no. 02, Mar. 2021, doi: 10.1142/S021759082043002X.

[3] Z. X. Wang, Z. W. Wang, and Q. Li, "Forecasting the industrial solar energy consumption using a novel seasonal GM(1,1) model with dynamic seasonal adjustment factors," *Energy*, vol. 200, p. 117460, Jun. 2020, doi: 10.1016/J.ENERGY.2020.117460.

[4] L. Kumar, M. Hasanuzzaman, and N. A. Rahim, "Global advancement of solar thermal energy technologies for industrial process heat and its future prospects: A review," *Energy Convers Manag*, vol. 195, pp. 885–908, Sep. 2019, doi: 10.1016/J.ENCONMAN.2019.05.081.

[5] L. A. Weinstein, J. Loomis, B. Bhatia, D. M. Bierman, E. N. Wang, and G. Chen, "Concentrating Solar Power," *Chem Rev*, vol. 115, no. 23, Dec. 2015, doi: 10.1021/acs.chemrev.5b00397.

[6] N. Boerema, G. Morrison, R. Taylor, and G. Rosengarten, “High temperature solar thermal central-receiver billboard design,” *Solar Energy*, vol. 97, Nov. 2013, doi: 10.1016/j.solener.2013.09.008.

[7] M. R. Rodríguez-Sánchez, A. Sánchez-González, C. Marugán-Cruz, and D. Santana, “New designs of molten-salt tubular-receiver for solar power tower,” *Energy Procedia*, vol. 49, pp. 504–513, 2014, doi: 10.1016/j.egypro.2014.03.054.

[8] A. El-Maddah, A. El-Amir, E. Ewais, and Y. Ahmed, “Sialon-based Composites for Solar Receivers: An overview,” *International Journal of Materials Technology and Innovation*, vol. 1, no. 1, Jun. 2021, doi: 10.21608/ijmti.2021.181126.

[9] D. Ngoue *et al.*, “Ceramics for concentrated solar power (CSP): From thermophysical properties to solar absorbers,” *Advanced Ceramics for Energy Conversion and Storage*, pp. 89–127, Jan. 2020, doi: 10.1016/B978-0-08-102726-4.00003-X.

[10] C. Heisel, C. Caliot, T. Chartier, S. Chupin, P. David, and D. Rochais, “Digital design and 3D printing of innovative SiC architectures for high temperature volumetric solar receivers,” *Solar Energy Materials and Solar Cells*, vol. 232, Oct. 2021, doi: 10.1016/j.solmat.2021.111336.

[11] G. J. Kolb, “SANDIA REPORT An Evaluation of Possible Next-Generation High-Temperature Molten-Salt Power Towers,” 2011. [Online]. Available: http://www.ntis.gov/help/ordermethods.asp?loc=7-4-0#online

[12] K. R. Zada, M. B. Hyder, M. Kevin Drost, and B. M. Fronk, “Numbering-Up of Microscale Devices for Megawatt-Scale Supercritical Carbon Dioxide

Concentrating Solar Power Receivers," *J Sol Energy Eng*, vol. 138, no. 6, Dec. 2016, doi: 10.1115/1.4034516.

[13] F. A. Al-Sulaiman and M. Atif, "Performance comparison of different supercritical carbon dioxide Brayton cycles integrated with a solar power tower," *Energy*, vol. 82, pp. 61–71, Mar. 2015, doi: 10.1016/j.energy.2014.12.070.

[14] P. Garg, P. Kumar, and K. Srinivasan, "Supercritical carbon dioxide Brayton cycle for concentrated solar power," *J Supercrit Fluids*, vol. 76, pp. 54–60, Apr. 2013, doi: 10.1016/j.supflu.2013.01.010.

[15] C. K. Ho and B. D. Iverson, "Review of high-temperature central receiver designs for concentrating solar power," *Renewable and Sustainable Energy Reviews*, vol. 29, Jan. 2014, doi: 10.1016/j.rser.2013.08.099.

[16] M. T. Luu, D. Milani, R. McNaughton, and A. Abbas, "Dynamic modelling and start-up operation of a solar-assisted recompression supercritical CO 2 Brayton power cycle," *Appl Energy*, vol. 199, Aug. 2017, doi: 10.1016/j.apenergy.2017.04.073.

[17] A. Fritsch, C. Frantz, and R. Uhlig, "Techno-economic analysis of solar thermal power plants using liquid sodium as heat transfer fluid," *Solar Energy*, vol. 177, Jan. 2019, doi: 10.1016/j.solener.2018.10.005.

[18] S. Awasthi and J. L. Wood, "Carbon/Carbon Composite Materials for Aircraft Brakes," doi: 10.1002/9780470310496.ch4.

[19] M. Ghalandari, A. Maleki, A. Haghighi, M. Safdari Shadloo, M. Alhuyi Nazari, and I. Tlili, "Applications of nanofluids containing carbon nanotubes in solar

energy systems: A review," *J Mol Liq*, vol. 313, p. 113476, Sep. 2020, doi: 10.1016/J.MOLLIQ.2020.113476.

[20] D. H. A. Besisa and E. M. M. Ewais, "Black zirconia composites with enhanced thermal, optical and mechanical performance for solar energy applications," *Solar Energy Materials and Solar Cells*, vol. 225, Jun. 2021, doi: 10.1016/j.solmat.2021.111063.

[21] A. P. Ilyushchanka, A. K. Kryvanos, O. A. Prokhorov, and M. U. Kryvulenka, "Optimization in the multi-cycle densification technology for manufacturing of the high density carbon fiber reinforced carbon," in *Journal of Physics: Conference Series*, Institute of Physics Publishing, Jul. 2020. doi: 10.1088/1742-6596/1507/6/062012.

[22] S. Wenxun, H. Yudong, Z. Zhiqian, and W. Junshan, "Influence of Graphitization Processing Upon the Carbon-Carbon Composite Interfacial Properties," 1997.

[23] C. K. Ho, "Computational fluid dynamics for concentrating solar power systems," *Wiley Interdiscip Rev Energy Environ*, vol. 3, no. 3, pp. 290–300, 2014, doi: 10.1002/wene.90.

[24] M. I. Roldán, J. Fernández-Reche, L. Valenzuela, A. Vidal, and E. Zarza, "CFD Modelling in Solar Thermal Engineering," pp. 1–38, 2015, [Online]. Available: www.IEEFoundation.org

[25] X. Xu *et al.*, "Experimental Test of Properties of KCl-MgCl2 Eutectic Molten Salt for Heat Transfer and Thermal Storage Fluid in Concentrated Solar Power Systems," *Journal of Solar Energy Engineering, Transactions of the ASME*, vol. 140, no. 5, Oct. 2018, doi: 10.1115/1.4040065.

[26] N. Boerema, G. Morrison, R. Taylor, and G. Rosengarten, “Liquid sodium versus Hitec as a heat transfer fluid in solar thermal central receiver systems,” *Solar Energy*, vol. 86, no. 9, pp. 2293–2305, 2012, doi: 10.1016/j.solener.2012.05.001.

[27] J. C. Cordeiro, R. E. Davis, H. Ramsurn, D. W. Crunkleton, T. P. Otanicar, and M. W. Keller, “Prediction of curing kinetics of resorcinol-added resole phenolic resins using differential scanning calorimetry for the fabrication of carbon/carbon composites,” *J Appl Polym Sci*, vol. 139, no. 39, Oct. 2022, doi: 10.1002/app.52949.

[28] A. P. Esser-Kahn *et al.*, “Three-Dimensional Microvascular Fiber-Reinforced Composites,” *Advanced Materials*, vol. 23, no. 32, pp. 3654–3658, Aug. 2011, doi: 10.1002/adma.201100933.

[29] J. A. Duffie and W. A. Beckman, *Solar Engineering of Thermal Processes*, 3rd editio. Wiley & Sons, Incorperated, 2006.

[30] A. Ambrosini, A. Boubault, C. K. Ho, L. Banh, and J. R. Lewis, “Influence of application parameters on stability of Pyromark® 2500 receiver coatings,” *AIP Conf Proc*, vol. 2126, no. July, 2019, doi: 10.1063/1.5117514.

[31] A. Boubault, J. Yellowhair, and C. K. Ho, “Design and Characterization of a 7.2 kW Solar Simulator,” *Journal of Solar Energy Engineering, Transactions of the ASME*, vol. 139, no. 3, pp. 1–8, 2017, doi: 10.1115/1.4036411.

[32] C. W. Ohlhorst, W. L. Vaughn, P. O. Ransone, and H.-T. Tsou, *Thermal Conductivity Database of Various Structural Carbon-Carbon Composite Materials*. Linthicum Heights: Nasa Center for AeroSpace Information, 1997.

[33] D. D. Baker, “Thermal Characterization of Carbon Composites,” North Carolina Agricultural and Technical State University, 2011.

[34] H. M. Hsiao and I. M. Daniel, “Strain rate behavior of composite materials,” *Compos B Eng*, vol. 29, no. 5, pp. 521–533, Sep. 1998, doi: 10.1016/S1359-8368(98)00008-0.

[35] J. K. Fink and L. Leibowitz, “Thermophysical Properties of Sodium,” May 1979.

[36] E. W. Lemmon, M. O. McLinden, and D. G. Friend, *Thermophysical Properties of Fluid Systems*. NIST Chemistry WebBook.

[37] J. E. Sheehan, K. W. Buesking, and B. J. Sullivan, “CARBON-CARBON COMPOSITES,” 1994.

[38] J. Coventry and P. Burge, “Optical properties of Pyromark 2500 coatings of variable thicknesses on a range of materials for concentrating solar thermal applications,” 2017, p. 030012. doi: 10.1063/1.4984355.

[39] G. Augsburger and D. Favrat, “Modelling of the receiver transient flux distribution due to cloud passages on a solar tower thermal power plant,” *Solar Energy*, vol. 87, no. 1, pp. 42–52, 2013, doi: 10.1016/j.solener.2012.10.010.

[40] S. M. Besarati, D. Yogi Goswami, and E. K. Stefanakos, “Optimal heliostat aiming strategy for uniform distribution of heat flux on the receiver of a solar power tower plant,” *Energy Convers Manag*, vol. 84, pp. 234–243, Aug. 2014, doi: 10.1016/j.enconman.2014.04.030.

[41] W. Q. Wang, Y. Qiu, M. J. Li, F. Cao, and Z. Bin Liu, “Optical efficiency improvement of solar power tower by employing and optimizing novel fin-like

receivers," *Energy Convers Manag*, vol. 184, no. August 2018, pp. 219–234, 2019, doi: 10.1016/j.enconman.2018.12.029.

[42] M. Astolfi, M. Binotti, S. Mazzola, L. Zanellato, and G. Manzolini, "Heliostat aiming point optimization for external tower receiver," *Solar Energy*, vol. 157, pp. 1114–1129, Nov. 2017, doi: 10.1016/j.solener.2016.03.042.

[43] J. I. Burgaleta, S. Arias, and D. Ramirez, "Gemasolar, the first tower thermosolar commercial plant with molten salt storage," *Solarpaces*, no. September, pp. 1–8, 2011.

[44] W. Ding and T. Bauer, "Progress in Research and Development of Molten Chloride Salt Technology for Next Generation Concentrated Solar Power Plants," *Engineering*, vol. 7, no. 3, pp. 334–347, 2021, doi: 10.1016/j.eng.2020.06.027.